

Magnetic Characterization of $\text{Y}_{2-x}\text{Bi}_x\text{Ir}_2\text{O}_7$: A Muon Spin
Rotation/Relaxation and Susceptibility Study

MAGNETIC CHARACTERIZATION OF $Y_{2-x}Bi_xIr_2O_7$: A MUON
SPIN ROTATION/RELAXATION AND SUSCEPTIBILITY STUDY

By

TERESA MEDINA FERNANDEZ, B.Sc. (HONS.)

A Thesis

Submitted to the School of Graduate Studies
in Partial Fulfilment of the Requirements
for the Degree
Master of Science

McMaster University

© Copyright by T. Medina Fernandez, September 2014

MASTER OF SCIENCE (2014)
(Department of Physics and Astronomy)

McMaster University
Hamilton, Ontario

TITLE: Magnetic Characterization of $Y_{2-x}Bi_xIr_2O_7$: A Muon Spin Rotation/Relaxation and Susceptibility Study

AUTHOR: Teresa Medina Fernandez, B.Sc. (Hons.)

SUPERVISOR: Graeme M. Luke

NUMBER OF PAGES: xii, 105

Abstract

Pyrochlore iridates have received considerable attention for the past few years as they possess strong electron correlations and spin orbit coupling, giving rise to a finite temperature metal-insulator transition (MIT). The nature of this MIT transition is related to the magnetic order of the Ir atoms which also experience frustration as they are part of a pyrochlore structure. The aim of this study is to elucidate the magnetic configuration of the magnetic iridium ions by doping $\text{Y}_2\text{Ir}_2\text{O}_7$ with Bi. Here we present a study on the magnetic properties of the $\text{Y}_{2-x}\text{Bi}_x\text{Ir}_2\text{O}_7$ ($x = 0, 0.2, 0.4, 0.9, 1.3, 2$) system using μSR and DC susceptibility.

Our results show that pure $\text{Y}_2\text{Ir}_2\text{O}_7$ has a magnetic transition to a long-range ordered state. Substituting Bi by Y results in a lower temperature transition with increasing amount of bismuth. When the system goes into the ordered state a weak ferromagnetic moment is seen. This is in agreement with the belief that the system orders in an canted antiferromagnetic fashion with all-in all-out spins in the tetrahedron of the pyrochlore structure. However the addition of bismuth into the sample does not change the internal magnetic field measured at low temperatures with μSR , but only changes the transition temperature and the ordered volume fraction.

For the $\text{Bi}_2\text{Ir}_2\text{O}_7$ system two magnetic transitions had been measured previously counter to the belief that this material did not order magnetically. In this work, our μSR measurements show no evidence of such a transition. In the transverse field μSR set up a small Knight shift is measured due to the local susceptibility of $\text{Bi}_2\text{Ir}_2\text{O}_7$.

Acknowledgments

This thesis and the work and the previous work that made possible for me to write it, is all thanks to the people I work with, my family and my friends. I will first start by thanking all the wonderful people that I work with and collaborated with. A special thanks goes to my supervisor Prof. Graeme Luke for his help, guidance and tireless work. If I've been the perpetrator of this work he for sure has been the captain of this enterprise. My group members: Travis Williams, Robert D'Ortenzio, Timothy Munsie, Anna Millington, Murray Wilson and Allanah Hallas. All of you have aided me with my work, answering all my questions and sharing with me your knowledge. They say it take an entires village to raise a child. After this experience I can say that it takes a whole group to write a thesis. I want to also thank from the bottom of my heart the help, support, counsel, guidance and mentorship of two wonderful friends and co-workers Hanna Dabkowska and Anthony Dabkowski. Many more people have helped me in this process. At McMaster University, Paul Dube has been a great help as well as John Greedan for his guidance and knowledge. At TRIUMF I can not forget the wonderful group I had the pleasure to work with and spend many overnight shifts with. The Columbia University group, with Prof. Yasutomo Uemura with which has been a pleasure to collaborate with, including his wonderful students: Benjamin Frandsen, Lian Liu, Carlos Arguello and Sky Cheung. Many things could have gone wrong while doing the experiments but they didn't because of all the great scientists that work at TRIUMF like Bassam Hitti, Donald Arseneau, Gerald Morris and Rahim Abasalti. Also I need to thank Ian Fisher's group for providing me with amazing samples to work with.

As important as the support and help to do the research, moral support is essential for this kind of projects. My friends that have been by my side in the good and the bad that have celebrated my triumphs and lifted my spirits in my down times. They have endured my singing, craziness and my weirdness. Kayla Fenton, Casey Marjerrison and Chandal, Stephanie Kedzior and Anna Millington. Although in the distance, my good friends Usue Zubia, Jasone Garay and Blanca Laso have been as always my constant source of support and happiness. The Lavelle family that has become my second family I thank you for all that you have given me and teach me. My family has been there supporting me since the very beginning. My aunt and godmother Lourdes Fernandez has always been an inspiration and a mentor for me. To my parents, Antonio Medina and Elena Fernandez, and brother Juan Medina (and Lola) to whom I dedicate this thesis, I can not thank you enough. It is thanks to you that I've become the woman I am now, able to take this project to a safe port. You are the fuel of my life, my hope, my happiness and I want to make you proud.

Even if I didn't mention their names there are countless other people that help and supported me along the way, inside and outside the lab. I thank you all for your support in whatever way it came and I will never forget.

Thank you.

Co-authorship

The work presented in this thesis is a collaborative work between me and other wonderful scientists.

μSR data collection at TRIUMF was done in collaboration with T.J. Williams, R. D'Ortenzio, T.J.S. Munsie, M. Wilson, A. Hallas from McMaster University as well as B. Frandsen, T. Goko, L. Liu and Y.J. Uemura from Columbia University. Magnetisation measurements were done with the help of P. Dube and X-ray diffraction measurements and refinement were done with the support and guidance of C. M. Thompson, C. Marjerrison and H. A. Dabkowska from McMaster University. The samples used in this work were made by M.C. Shapiro, S.C. Riggs and I.R. Fisher at Stanford University and M. B. Stone at Oak Ridge National Laboratory.

Finally the analysis and the composition of this thesis were my own work under the supervision of G.M. Luke.

Contents

| | | |
|----------|--|-----------|
| 1 | Introduction - Overview of $Y_{2-x}Bi_xIr_2O_7$ | 1 |
| 1.1 | Magnetic properties and magnetic frustration in crystalline samples | 2 |
| 1.2 | Pyrochlore iridates and previous work on pyrochlore iridates . | 6 |
| 1.3 | Yttrium iridate doped with bismuth | 11 |
| 2 | Experimental techniques | 15 |
| 2.1 | Radio frequency Superconducting Quantum Interference Device (RF SQUID) | 15 |
| 2.1.1 | Superconductors and Meissner effect | 16 |
| 2.1.2 | SQUIDs theory | 17 |
| 2.1.3 | RF SQUID magnetometer | 19 |
| 2.2 | X-ray powder diffraction | 21 |
| 3 | Muon Spin Rotation, Relaxation and Resonance (μSR) | 27 |
| 3.1 | Principles of μ SR | 27 |
| 3.2 | Zero/Longitudinal Field set up | 31 |
| 3.3 | Transverse Field geometry | 37 |
| 4 | Results | 41 |
| 4.1 | Susceptibility | 42 |
| 4.1.1 | FC and ZFC at 1T | 42 |
| 4.1.2 | FC at 100G | 46 |
| 4.2 | X-ray Analysis and Rietveld refinement | 47 |

| | | |
|----------|---|-----------|
| 5 | μSR results | 57 |
| 5.1 | $Y_{2-x}Bi_xIr_2O_7$ results | 57 |
| 5.1.1 | Zero field | 58 |
| 5.1.2 | Weak transverse field and transversed field | 62 |
| 5.2 | $Bi_2Ir_2O_7$ results | 64 |
| 6 | Conclusions and future work | 71 |
| 6.1 | Prospective future work | 73 |
| | Bibliography | 77 |

List of Figures

| | | |
|-----|--|----|
| 1.1 | Antiferromagnetically coupled spins show geometrical frustration where all the spins can not be antiparallel to all their neighbours at the same time. This kind of frustration can happen in either a) a two dimensional lattice or b) a three dimensional lattice. | 4 |
| 1.2 | When adding the triangular motives from figure 1.1 a) two dimensional lattices are form in which frustration is present. Some examples are a) triangular lattice and b) Kagome lattice. | 4 |
| 1.3 | A cubic pyrochlore lattice is form when adding corner shearing tetrahedral from figure 1.1 b). Consequently there can be geometric frustration. In this figure only the A-site sub lattice is shown. | 5 |
| 2.1 | Dependence of the total flux on the SQUID, Φ_0 in terms of the externally applied flux, Φ_a . [Clarke 2006] | 17 |
| 2.2 | Schematic of a copper pairs tunnelling through a normal metal in a S-M-S junction. When an electron is scattered between the two superconductors it will be absorbed by the superconductors. That electron will pair with another electron emitting at the same time a hole that will break a cooper pair of the other superconductor emitting another electron to maintain time reversal symmetry. This process then will go on transporting cooper pairs from one superconductor to the other. | 18 |
| 2.3 | Radio frequency (rf) and dc (left and right) SQUIDs. The convention is to indicate the Josephson junctions with a X. As it can be seen the RF SQUID posses only one Josephson junction and there is no voltage difference applied to it. Meanwhile the dc SQUID has two Josephson junctions and there is an external dc voltage applied to the SQUID. [Clarke 2006] | 19 |
| 2.4 | Schematics of the RF SQUID cryogenics system [Design 2013]. | 21 |
| 2.5 | Schematic of the geometry of the X-ray diffractometer: (1) collimator, (2) powder sample mounted in the goniometer and (3) detector. The precision of angles is of the highest importance in diffraction measurements so a goniometer is used so assure that high precision. | 25 |

-
- 3.1 Muons production and decay is governed by the weak interaction. a) the parity violation makes the muons be emitted 100% polarised with the muon spin pointing opposite to their momenta thus conserving the linear momentum of the pion. b) when the polarised muon decays into a positron and two neutrinos the positron is emitted asymmetrically, but there is a higher probability of the positron to be emitted in the direction of the muon spin. [Sonier] 30
- 3.2 One of the experimental set ups use in μSR is the longitudinal field (LF) set up. In this experimental geometry the externally applied field is applied along the direction of the muon spin momentum. A variation of this set up is zero field (ZF) as shown in this figure. A muon enters and is detected by a scintillation detector starting a digital clock. The muon will then enter the sample and interact with the internal local field. When the muon decays only the positron will be detected by the one of the two scintillation detectors stopping the clock and creating an event at a certain time. [Sonier] 32
- 3.3 The top diagram shows a raw histogram measured from a detector from a measurement done on a sample with an internal local field. The oscillation of the signal reflects the oscillations of the muon inside the sample. The decay of the counts is due to the muon lifetime. In the asymmetry spectrum at the bottom is created by subtracting the histogram of two opposing counters and dividing it by the addition of the two same counter's asymmetry. This gives the behaviour of the muon without the decay due to the lifetime of the muon [Kreitzman 1999] 33
- 3.4 This schematic shows how the muon's spin in this case in the z direction interacts with the local internal field \mathbf{H}_{loc} . If the angle ϑ is different from zero then the muon spin will precess around the field. Equation 3.4 defines the spin polarisation. 34
- 3.5 In the transversed field (TF) set up an external field is applied perpendicular to the muon spin polarisation direction. The muon is detected as it enters the sample by a thin muon detector that starts the digital clock that will stop when the positron is detected after it is created from the muon decay. For this experimental configuration the two most used pair of detectors are the up or down and left and right. [Sonier] 37
- 3.6 Schematics of the coordinate system and labelling used in μSR . The beam will always be in the z direction. In both the longitudinal field (and zero field) as well as the weak transversed field the muon's spins point in the z direction while for the transversed field the spins are rotated to point x direction. [Kreitzman 1999] 39

-
- 4.1 Magnetic susceptibility on the powder samples $Y_{2-x}Bi_xIr_2O_7$ $x = 0, 0.2, 0.4, 0.4(2), 0.9, 1.3$ and 2 in a 1 T field. A zero field cooled (ZFC) and a field cooled (FC) measurement was done for every sample. The departure of the ZFC and ZF signals marks the transition to an magnetically ordered state (see table 4.3). This difference shows a small magnetic moment due to a weak ferromagnetic order which is in agreement with the picture of canted antiferromagnetic order. The $Bi_2Ir_2O_7$ sample does not have a transition as the ZFC and FC signals do not depart from each other. When carrying the measurement on the SQUID magnetometer each point is measured over a small amount of time (~ 2 minutes). This amount of time allows to the spins to align with the external field even in ZFC run. This created the small peak seen for $x = 0.2$ and 0.9 samples at 140 K and 110 K respectively. The peaks mark with an asterisk (*) correspond to oxygen peaks trapped in the sample cavity at the time of the measurement. 50
- 4.2 Inverse of the susceptibility from the 1 tesla measurements shown in Fig.4.1. A Curie-Weiss (black line) law has been fitted to find the Néel temperature of the four samples. The inverse of the susceptibility of the whole temperature is plotted in the inset. 51
- 4.3 Comparison of the field cooled magnetic susceptibility at 100 G (full circle) and 10000 G (empty circle) applied field vs. temperature on the transition temperature regime on the doped samples $x = 0.2, 0.4, 0.9$ and 1.3. There seems to be a change to the transition temperature with field for some samples. But it can be seen that there is a decrease in the susceptibility with increasing field. 52
- 4.4 The X-ray refinement shows that the higher doped samples did not have the desired amount of bismuth. The total amount of bismuth was not fully accepted by the pyrochlore lattice and thus the lattice parameter was smaller than expected. In this figure the actual amount of bismuth can be approximated by extending lines (dotted lines) to the fit line (solid line). 53

-
- 4.5 Powder-diffraction data (circle) of the two $x = 0.4$ samples measured at room temperature. The red solid line shows the Rietveld refinement and with the blue solid line it can be seen the difference between the observed and the calculated refinement. The vertical sticks show the position of the peaks. Both refinement shows that the results are consistent. In both cases there is a small amount of unreacted Y_2O_3 which peaks are indicated with the yellow circle. For one of the samples a silicon standard (green star) was added to check the correct alignment of the diffractometer. 54
- 4.6 Powder-diffraction data (circle) of the $x = 0.2$ (top) and fully doped $Bi_2Ir_2O_7$ (bottom) measured at room temperature. The red solid line shows the Rietveld refinement and the blue solid line shows the difference between the observed and the calculated refinement. The vertical sticks show the position of the peaks. The $Bi_2Ir_2O_7$ sample has no sign of secondary phases showing a great quality sample. Meanwhile the $Y_2Ir_2O_7$ and $Y_{1.8}Bi_{0.2}Ir_2O_7$ samples have some yttrium oxide unreacted left in them indicated by the yellow circles. 55
- 4.7 The powder-diffraction data of the $Bi_2Ir_2O_7$ is here compared with a database calculated pattern showing a great agreement between the two. There is no evidence of any secondary magnetic phases. 56
- 5.1 (Colour lines) Zero field μSR data with fits to Eq. 5.1 of the pure $Y_2Ir_2O_7$ and the doped sample $x = 0.2$. (a) shows the behaviour of both samples above the transition temperature (200 K) where no sign of magnetic is observed as expected in the paramagnetic regime. (b) Below the transition temperature (2 K) the oscillation observed in both samples indicates the presence of internal magnetic field. For the low temperature graph only the first microsecond was plotted with the purpose of making the oscillations more clear to the eye. This two samples are the only ones that show evidence of internal magnetic field bellow the transition temperature. 59
- 5.2 Temperature dependence of the frequency parameter obtain from the fitting of the μSR data using Eq. 5.1 as shown in Fig.5.1. It can be seen that the frequency does not change with the input of bismuth but the transition temperature decreases. This order parameter is fitted using a phenomenological equation $\langle B_{loc} \rangle \sim [1 - (T/T_c)^\alpha]^\beta$ 61

-
- 5.3 Asymmetry derived from the fitting of the μSR weak transverse field data using equation 5.2 for the $x = 0.2$ and 0.4 . The dotted line is a guide to the line to see the value of the asymmetry above the transition temperature where all the sample is the paramagnetic. The rest of the doped samples which were determined of not good quality ($x = 0.9$ and 1.3) are shown in the inset of the graph to compare. 63
- 5.4 Zero field μSR data of the fully doped bismuth iridate that was been fitted to Eq. 5.3. For comparison the higher temperature (5 K) and the lower temperature (30 mK) measured have been plotted together and it can be seen that there is no difference between them. There is no evidence of a transition to an ordered state. 65
- 5.5 Plot of the relaxation (λ) obtain from the fitting of the zero field μSR data of the $\text{Bi}_2\text{Ir}_2\text{O}_7$ using equation 5.3. The relaxation shows no evidence of a transition temperature 66
- 5.6 1tesla transversed field μSR data with fits to equation 5.2 on $\text{Bi}_2\text{Ir}_2\text{O}_7$. Plotted are the 5 K and 30 mK signals for a comparison. No difference can be seen between the two samples confirming the absence of transition into a ordered state. . . . 67
- 5.7 Parameters derived from fitting the data in Fig.5.6 using equation 5.2. (a) In the frequency vs. temperature a flat profile is seen except for the point at 5 K that seems to be a little higher due to the magnetic field not being stabilised. (b) To check approximately what was the field that was being applied to the sample, the hall probe measurement is plotted against temperature to see the field value at each moment. It can be seen that the value of the field at 5K is a little higher that expected. (c) To see if the field stabilisation affected the measurements, the ratio of the frequency over the Hall probe reading is plotted against the temperature. The linear increase shows that thought the value of the field was not the correct one, the Knight shift increases with temperature is smooth an proportional to the internal field induced. 68
- 5.8 (a) The increase of the relaxation of the μSR data with decreasing temperature indicates a broadening of the angular variation in the susceptibility which is proportional to the internal inhomogeneous field. (b) In the frequency-Hall probe ratio vs. relaxation plot it can be seen that the knight shift is proportional to the broadening. This means that the broadening increases with the shift. 69

- 6.1 Phase diagram of $R_2Ir_2O_7$ based on R site ionic radius dependence of the metal-insulator transition and magnetic transition temperature. 73
- 6.2 Plot of the magnetic susceptibility on the $Bi_2Ir_2O_7$ in 100 G, 500 G, 10 KG and 40 KG fields. Zero field cooled (ZFC) or field cooled (FC) measurement were done at those fields but in the case of 1 T were both FC and ZFC measurements were taken. A distinct turn over is observed for three of the four fields measured. The inset shows the behaviour of this sample at high temperatures for each of the fields. 75

Introduction - Overview of



Contents

| | | |
|-----|---|----|
| 1.1 | Magnetic properties and magnetic frustration in crystalline samples | 2 |
| 1.2 | Pyrochlore iridates and previous work on pyrochlore iridates | 6 |
| 1.3 | Yttrium iridate doped with bismuth | 11 |

In this work the magnetic properties of the $Y_{2-x}Bi_xIr_2O_7$ system will be studied. As it will be explained later in this chapter, this family of materials has very interesting electric and magnetic properties. In this era of technology, where the fulfilment of many everyday tasks, the advance of society and the solution to many problems relies on the power of computers and technology, the advance in the understanding of magnetic systems is of the greatest importance.

1.1 Magnetic properties and magnetic frustration in crystalline samples

Magnetic frustration arises from competing interactions between magnetic moments in a crystal lattice. There are two causes of magnetic frustration. The first one is due to the geometry of the lattice and the second one is due to competing magnetic interactions of the unpaired electrons. In both cases the system is said to be frustrated when it can not reach the minimum classical energy by minimising the interaction energy of each spin pair-by-pair. The type of frustration most relevant for this work is the magnetic frustration in pyrochlore oxides due to geometrical frustration.

In a crystal the different ions are bonded forming the crystal lattice. Magnetically interesting materials are those that after the bonding, the ions still have unpaired electrons. In this case there is also a magnetic sublattice embedded in the lattice. One or more ion species can be magnetic; hence each of them generates a magnetic sublattice. In the case of many magnetic ion species there will be interactions between the different magnetic sublattices making the system more difficult for its study. This is why in many cases it is preferred to have a system in which there is only one magnetic ion in the lattice. In any case, the geometry of the sublattice and the strength of the interaction of the spins are very important to determine the magnetic behaviour of the system.

The possible magnetic interactions of a system can be either ferromagnetic or antiferromagnetic which favour parallel or antiparallel spin arrangements respectively. To describe the systems in the ordered states some mathematical models are used. Two of the most commonly used models are the Ising model

and the Heisenberg model. In the Ising model spins can only point up or down while in the Heisenberg model the spins can point in any direction. The following Hamiltonian is the Ising model Hamiltonian:

$$H = J \sum_{\langle i,j \rangle} S_i^z \cdot S_j^z. \quad (1.1)$$

The type of interaction is parametrised by the spin exchange parameter J and $S_i^z \cdot S_j^z$ represents a pair of spins that interact. If $J < 0$ the system will favour ferromagnetic order and antiferromagnetic if $J > 0$. A paramagnetic state occurs when there is a lack of magnetic interactions of the spins or at high temperatures when the thermal energy is larger than the spin interactions. In this state the spins point in random directions and fluctuate, so there is no magnetic order, hence no net magnetic moment in the absence of an external field. All systems are paramagnetic above their transition temperature even if below they go to an ordered state (ferromagnetic or antiferromagnetic). Magnetic frustration can inhibit the magnetic order and prolong the paramagnetic state below what would be the transition temperature.

The next step is discussing when magnetic frustration can occur. The simplest example of geometric frustration is given by the antiferromagnetic Ising system (Eq. 1.1). To simplify the model it is common to take the interaction ($J > 0$) to be the same for all pairs of spins. Geometrical frustration is fulfilled in Ising system when the spins lie on the vertices of a triangle or a tetrahedron as seen in Fig. 1.1. The three spins at each corner are unable to align antiparallel to each other at the same time. When this triangular motifs are put together to form 2D (Fig. 1.2) and 3D (Fig. 1.3) lattices, the spins in the lattice are unable to order, preventing the system

from reaching an ordered state [Gardner 2010].

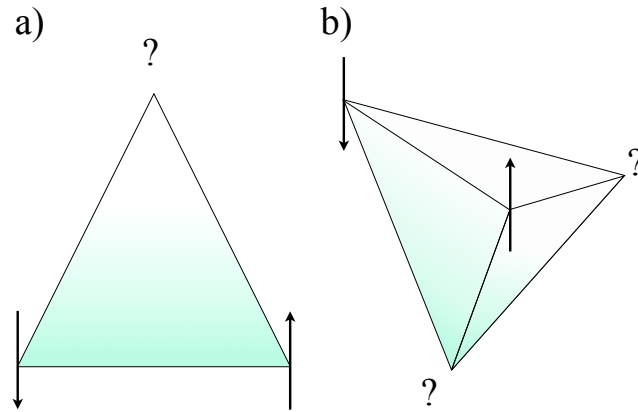


Figure 1.1: Antiferromagnetically coupled spins show geometrical frustration where all the spins can not be antiparallel to all their neighbours at the same time. This kind of frustration can happen in either a) a two dimensional lattice or b) a three dimensional lattice.

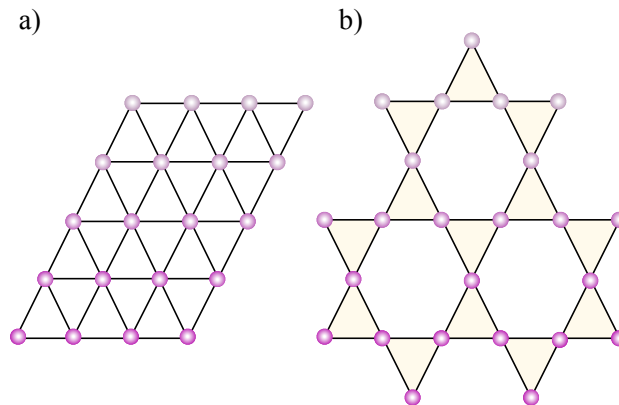


Figure 1.2: When adding the triangular motives from figure 1.1 a) two dimensional lattices are formed in which frustration is present. Some examples are a) triangular lattice and b) Kagome lattice.

An experimental way to characterize the level of frustration is the so-called frustration index f [Gardner 2010] or Ramirez ratio:

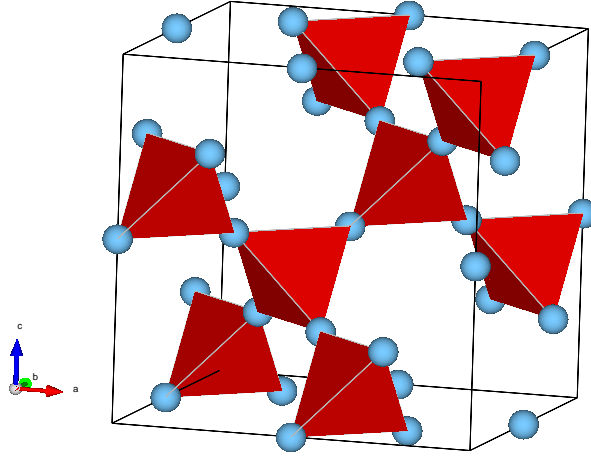


Figure 1.3: A cubic pyrochlore lattice is form when adding corner shearing tetrahedral from Fig. 1.1 b). Consequently there can be geometric frustration. In this figure only the A-site sub lattice is shown.

$$f = |\Theta_{CW}|/T_C \quad (1.2)$$

were Θ_{CW} is the Curie-Weiss temperature and T_C is the temperature at which the system goes into a long range ordered state. The Curie-Weiss temperature is obtained from the linear part at high temperature of the inverse susceptibility $\chi^{-1} \propto T - \Theta_{CW}$ [Gardner 2010] [Lacroix 2011]. The Curie-Weiss temperature is a good indicator of the type of interactions. For a negative Θ_{CW} the system behaves antiferromagnetically, whereas a positive Θ_{CW} indicates ferromagnetic behaviour. This high temperature regime is the paramagnetic regime. For a non frustrated material, the CW temperature is very similar to the transition temperature. On the other hand in the case of an ideal spin-liquid material, which has no long-range order down to 0 K, the Ramirez ration would be infinite. For frustrated materials though the two temperatures are different. Accordingly, the lower the T_C compared to Θ_{CW} the more

frustrated the system is.

The interest behind the study of geometrically frustrated pyrochlore oxide is that the frustration can lead to interesting quantum mechanical behaviours. For the pyrochlore structure $A_2B_2O_7$ some of the unconventional magnetic and thermodynamic behaviours would be: spin glass freezing, spin-liquid, ordered and disordered spin-ice, order by disorder, unconventional anomalous Hall effect, superconductivity and Kondo-like effect [Gardner 2010] .

1.2 Pyrochlore iridates and previous work on pyrochlore iridates

Transition-metal oxides with 5d orbitals have been of interest for the past few years. This interest is raised by the fact that the 5d orbital is relatively large. The electron correlations of this extended orbitals is hence of the same energy scale as the spin orbit coupling (SOC) and the crystal electric field [Dis-seler 2014]. This means that none of these interactions can be treated as a perturbation [Baker 2013]. The result is the appearance of very novel topological phases like Mott insulator and Weyl semimetal due to the competing energy scales. However magnetic order is predicted for the members of this system below the transition temperature. Magnetic order breaks time-reversal symmetry. This means that the possible phases cannot be topological insulators because they require time-reversal symmetry. Consequently the new topological semimetal phase was predicted for the pyrochlore iridates. The ground state of these materials is going to be determined by the interplay of these competing interactions. Therefore a small perturbation of the aforementioned interactions, like changes in the lattice parameters, can disrupt the

balance of the competing energies, thus change the ground state [Qi 2012].

Pyrochlores oxides ($A_2B_2O_7$) possess a cubic structure with space group $Fd\bar{3}m$. In the rare-earth pyrochlore iridates $R_2Ir_2O_7$ ($R=Y$ and rare-earth) in the case of the magnetic Ir^{4+} ions the unfilled band $5d^5$ is split by the crystal field into e_g band and the t_{2g} band. The SOC splits the t_{2g} the band further into a $J_{eff} = 1/2$ and a $J_{eff} = 3/2$ multiplet. Four of the five $5d$ electrons fill the lower $J_{eff} = 3/2$ quadruplet and one electron partially fills the $J_{eff} = 1/2$ doublet giving the iridium ions an effective $J = 1/2$ [Qi 2012]. The Ir ions form a corner sharing tetrahedral lattice (Fig. 1.3). This arrangement often introduces magnetic frustration. Due to the simultaneous presence of magnetic frustration and $5d$ transition-metal oxide elements, pyrochlore iridates present a great opportunity to study the interplay between the electronic correlations and magnetic frustration [Disseler 2012].

A very important matter is the interplay of the magnetic frustration and the electronic interactions (electron correlation, SOC and crystal electric field). One of the reasons the pyrochlores have been the focus of study for a long time is the hope of understanding how the magnetic frustration influences strongly correlated electron systems. Previous studies of iridate pyrochlores have revealed a finite temperature metal-insulator (MI) and a magnetic transition [Yanagishima 2001] [Matsuhira 2007]. In these works, the electrical resistivity shows a transition into an insulating state for all but Pr and Bi. From the resistivity it can be seen that $R = Pr, Nd, Sm, Eu$ and Gd exhibit metallic behaviour (no MI transition) whereas $R = Tb, Dy, Ho, Yb$ and Y exhibit non-metallic behaviour below the MI transition. On the other hand the susceptibility measured in the same samples shows a difference between the zero field-cooled (ZFC) and the field-cooled (FC) susceptibility below the

MIT. This indicates the presence of magnetic transition to an ordered insulating state at low temperatures [Matsuhira 2011]. Consequently, for the compounds with $R = Y$ or a lanthanide, the electrical resistivity and magnetic susceptibility show that the MIT and the magnetic transition are coupled as they share a transition temperature [Matsuhira 2011] [Fukazawa 2002]. At the same time, by changing the size of the R ion, the d-electron bandwidth becomes narrower until the MIT and the magnetic transition is suppressed for the praseodymium and bismuth compounds [Matsuhira 2011] [Yanagishima 2001]. Finally, another conclusion that was drawn from these results is that the magnetic signature below the transition is also present in the compounds with non-magnetic ions in the R site. Therefore the magnetic order must come from the magnetic iridium ion. In the case of magnetic R ions Matsuhira *et al.* [Matsuhira 2011] argues that the low temperature ($\lesssim 50$ K) increase of the susceptibility is due to the magnetic R ions or magnetic impurities.

The nature of the magnetic order and the ground state of these materials have been discussed intensely. For example, the inverse of the susceptibility of the pyrochlore iridates has been measured and fit to a Curie-Weiss law above the transition temperature, except for the cases of $\text{Sm}_2\text{Ir}_2\text{O}_7$ and $\text{Eu}_2\text{Ir}_2\text{O}_7$ [Yanagishima 2001] and $\text{Y}_2\text{Ir}_2\text{O}_7$ [Shapiro 2012]. For all the fittings, a negative Θ_{cw} has been found indicating an antiferromagnetic interaction. It is important to notice that other rare earth pyrochlores have been reported to order in a ferromagnetic manner e.g.: $\text{A}_2\text{Mn}_2\text{O}_7$ ($A = \text{Sc}, \text{Y}, \text{Lu}, \text{In},$ and Tl) and $\text{A}_2\text{Ti}_2\text{O}_7$ ($A = \text{Tb}, \text{Ho}$ and Yb) to name a few [Gardner 2010], giving another example on the important role that the Ir interactions play in the magnetic order of this family even in the case of magnetic R ions. The increase of the FC susceptibility compared with the ZFC, indicates the presence of a

weak ferromagnetic behaviour (similar to a ferrimagnetic behaviour). The magnetic moments found are very small ($\sim 10^{-3}\mu_B/f.u.$) [Matsuhira 2011] and so it is improbable that the MIT is caused by the weak ferromagnetic ordering. Therefore, the proposed origin for the MIT is either a spin glass or a canted antiferromagnetic ordering [Fukazawa 2002] [Matsuhira 2011].

Unless a microscopic probe is used, the magnetic order of this samples can not be uniquely identified. Accordingly, to unequivocally determine the magnetic structure of $R_2Ir_2O_7$, neutron scattering is the best probe. Due to the expected small moment of the Ir ($\sim 0.2\mu_B/Ir$ for $Q \neq 0$ and $\sim 0.5\mu_B/Ir$ for $Q = 0$ [Matsuhira 2011] [Disseler 2014]) the magnetic state is very difficult to study using this technique, hence so far it has not been possible to use neutron scattering for the study of this material. Luckily another microscopic probe can be used for this purpose Muon Spin Rotation, Relaxation and Resonance (μSR) (see chapter 3).

The results using μSR on the Y compound have shown evidence of long range order in zero field (ZF) measurements [Disseler 2012]. The measurements show a spontaneous muon precession indicative of internal local static magnetic field below the transition temperature. In the same paper, the authors were able to determine the order parameter of the magnetic phase by plotting the muon precession frequency vs. temperature. The order parameter shows the internal field that appears at the MIT and magnetic transition via a second order transition. This is so far the best evidence of long-range order. Some groups have tried to identify the magnetic order of $Y_2Ir_2O_7$. The proposed ordered spin structures were the all-in/all-out (AIAO), two-in/two-out (TITO), FM(111), FM(100) and a coplanar state with orthogonal spins due to the indirect Dzyaloshinsky-Moriya interactions for [Disseler 2012]. Dis-

seler *et al.* could not give a definite result for the spin structure due to the uncertainty in determining the muon-stopping site. However, the authors concluded that the only possible structures could be the AIAO, TITO and the collinear FM(111). A few years later Disseler, in his 2014 paper, gives three possible structures to consider: AIAO, spins rotated $\pi/2$ from the AIAO and a coplanar configuration for the spins [Disseler 2014]. In this work the Bayesian methods were used [Blundell 2012]. The basis of this method is to determine the probability distribution function of obtaining a certain moment for the Ir ions using the precession frequency observed in [Disseler 2012]. This method gave, for the AIAO configuration, a value ($\mu = 0.32\mu_B$) very close to the expected magnetic moment of the Ir ions $\langle\mu\rangle = gJ\mu_B = 1/3\mu_B$. After this, a more detailed comparison was done using calculated magnetic fields at the potential muon stopping sites, which were also calculated. The muon precession frequency was then calculated at those sites for each of the possible structures using the most probable magnetic moment from the previously mentioned calculation. After comparing this calculated frequencies with the actual frequencies measured for some of this materials, the agreement between the AIAO frequency (16.5 ± 0.2 MHz) and the actual measured frequency (14.9 ± 1.3 MHz) was remarkable. In other words, this calculations shown that the magnetic ground state that best agreed with the observed measurements of $\text{Y}_2\text{Ir}_2\text{O}_7$ (an the other members of the pyrochlore iridate family) is the AIAO structure of the Ir^{4+} with a $J_{eff} = 1/2$.

1.3 Yttrium iridate doped with bismuth

Yttrium iridate is a very interesting system to study, as the only atom with magnetic moment is the Ir. This allows the study of the iridium magnetic behaviour and structure without any influence of any other magnetic species.

$R_2Ir_2O_7$ pyrochlores possess a MIT as described in the previous section. As was also discussed in the previous section, the transition temperature to the magnetically ordered insulating state decreases as ionic radius increases until it disappears. Additionally, another suggested way of suppressing the magnetic order was by the substitution of the rare-earth ions by other ions [Greedan 1994]. This substitution will introduce disorder into the structure as well as modifying the lattice parameter as the ionic radius of the dopant will differ from the substituted ion. Thus, the substitution of the R ion gives an opportunity to study how the R site ion affects the properties of $R_2Ir_2O_7$ systems. It is then of interest to study possible correlations between the magnetic properties and the lattice parameter or ionic radius. However, not any atom can be used as a dopant in the pyrochlore iridates. There are only certain elements that can be put into the pyrochlore structure. The possible A and B site elements are listed in [Greedan 1994]. Two of those dopant options are calcium and bismuth. Fukazawa *et al.* published a study on the calcium doped yttrium iridate [Fukazawa 2002]. The authors report an induced MIT transition up to doping levels of about 15%. They observed the same splitting of the ZFC-FC of the susceptibility below $x = 0.3$ indicating a small ferromagnetic component. When doping the system with calcium, it is being doped with holes. This reduces the half filled t_{2g} band which results in the appearance of a finite density of states at the Fermi level, turning the

material metallic [Fukazawa 2002]. In the case of the bismuth doped yttrium iridate no holes are introduced to the system. When bismuth is introduced into the R site it becomes a closed $5d$ shell. A difference is that the Bi has a larger ionic radius ($r = 1.17 \text{ \AA}$) than Y ($r = 1.02 \text{ \AA}$) [Shannon 1976]. So in this case the tuning of the energy scales happens as the bismuth atoms introduces disorder into the system by spatially deforming the lattice. This is the same process that occurs when changing the R site ions from Y, Pr to Lu. Of course, by Bi doping the change of the R site ion is done gradually and it can be used to see at what point the change into the metallic phase happens.

It is interesting to notice that the physics of the pyrochlore iridates goes against traditional arguments. Following those arguments and based on the extended nature of the $5d$ orbitals of the $R_2Ir_2O_7$ pyrochlore it is expected not to be magnetic and rather to exhibit a metallic behaviour. As shown earlier this is far from what has been observed except for the $Bi_2Ir_2O_7$ [Qi 2012]. The bismuth pyrochlore gives the opportunity to study the physics of the pyrochlore iridates with a non-magnetic ion in the R site but different from the yttrium iridate. Bismuth is the pyrochlore with biggest lattice constant as bismuth is the largest ion that can be placed on the R site. In comparison with $Y_2Ir_2O_7$ it can be used to see how the change of lattice parameter affects the magnetic properties. Previous work have shown that $Bi_2Ir_2O_7$ remains metallic down to 2 K with no anomalies in the susceptibility, specific heat or electrical resistivity suggestive of any presence of long-range order down to 50 mK [Qi 2012]. This metallic behaviour is due to the hybridisation of the $6s/6p$ Bi orbitals with the $5d$ orbital of the iridium atom. The energy of this hybridisation is much greater than the other electronic interactions (SOC and electron correlation) which can be seen as perturbations driving the system

into a metallic state [Qi 2012]. In a more recent work, Baker *et al.* observed a magnetic transition at 1.84(3) K and a further transition at 0.23(4) K using μSR . The results show an increase of the muon spin relaxation rate at those reported temperatures [Baker 2013]. They propose that the first transition at 1.84 K could be the transition to a quasimagnetic state while the nature of the second transition remains unknown. Baker and coworkers report a small field seen by the muons of 0.7 mT suggesting that an ordered state may exist. This field is much smaller in comparison with the yttrium compound and the other prochloro iridates. The magnetic moment they suggest is $\sim 0.01\mu_B/\text{Ir}$ which agrees with the saturation of the magnetisation reported by Qi *et al.* A new weakly antiferromagnetic metal low temperature state was suggested for $\text{Bi}_2\text{Ir}_2\text{O}_7$.

After this review it can be seen that considerable work had been done in characterising electric properties and magnetisation of these materials. Some attempts to measure the magnetic structure by neutron diffraction have been done but none of them successfully as the moment of the iridium is very small, which combined with the powder form of the available samples make such studies extremely difficult. It is then very important that a μSR study in this material is done.

Experimental techniques

Contents

| | | |
|------------|---|-----------|
| 2.1 | Radio frequency Superconducting Quantum Interference Devise (RF SQUID) | 15 |
| 2.1.1 | Superconductors and Meissner effect | 16 |
| 2.1.2 | SQUIDs theory | 17 |
| 2.1.3 | RF SQUID magnetometer | 19 |
| 2.2 | X-ray powder diffraction | 21 |

2.1 Radio frequency Superconducting Quantum Interference Devise (RF SQUID)

SQUIDs are based on flux quantisation physics and are the most sensitive magnetometers available. The RF SQUID consists of a superconducting loop with a single weak-link that is inductively coupled via a mutual inductance M to an rf current driven inductor capacitor (LC) tank circuit. When the tank circuit is biased with an rf current, the rf voltage across the tank circuit depends quite sensitively on the magnetic flux applied to the SQUID loop. This sensitivity is due to the non-linearity of the junction that results in a

change of the impedance in the rf circuit and hence a change of the amplitude of the rf voltage across the tank circuit that can be measure. RF SQUID magnetometers are widely used thanks to their high sensitivity.

2.1.1 Superconductors and Meissner effect

One characteristic of a superconducting state is that it can be described by a macroscopic wave function [Tinkham 2012]. Another characteristic is the Meissner effect which is based on perfect diamagnetic behaviour. In the case of having a superconducting loop, the same principles apply. The same wave function will be found through out the inside of the superconducting loop and fields will be repelled from going inside the sample. The difference is that now things can happen at the hole which is in the middle of the loop. For example, if a magnetic field is applied to the loop, the field will be able to go through the hole and thus a flux will appear inside the hole. The flux through the loop is quantised [Tinkham 2012] as the superconducting wave function has to have a unique value at any place on the superconductor ring; it is single valued. The spectrum of flux is quantised in integer numbers of flux quanta Φ_0 instead of being a continuum spectrum [Clarke 2006]. That quantisation condition is:

$$\Phi_T = n\Phi_0 \quad \Phi_0 = \frac{h}{2e} \quad (2.1)$$

This means that the superconducting wavefunction can only change phase by 2π when going around the ring.

If a magnetic flux is applied (Φ_{ext}) to the superconducting loop a superconducting current (screening current) would rise inside the superconductor that would create an opposite flux Φ_T that would cancel the flux through

the hole. That would be the case of perfect screening situation: $\Phi_{ext} = \Phi_T$ (straight line in Fig. 2.1). The same flux to the applied flux has been induced in the loop. On the contrary on a RF SQUID (and also in the dc SQUIDS) the screening is not perfect because of the presence of the JJ [Clarke 2006]. The screening current tries to screen the applied flux but because of the JJ allows a phase difference.

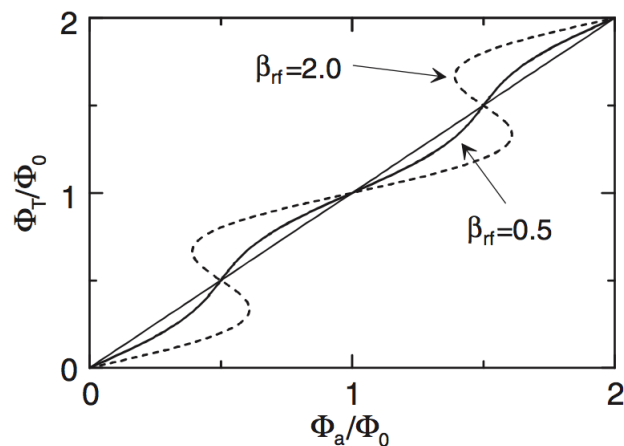


Figure 2.1: Dependence of the total flux on the SQUID, Φ_0 in terms of the externally applied flux, Φ_a . [Clarke 2006]

2.1.2 SQUIDS theory

There are two types of Superconducting Quantum Interference Devices (SQUIDS): dc and radio-frequency (rf). The dc SQUID has two Josephson junctions (JJ) in the loop connected in parallel and the superconducting loop is biased with a dc current [Clarke 2006]. The other type of SQUID is the RF SQUID. This type of device has only one JJ in the conducting loop and it is biased with a radio frequency current. The Josephson junction has a weak link, through which supercurrent tunnels between two superconductors

as shown in figure 2.2.

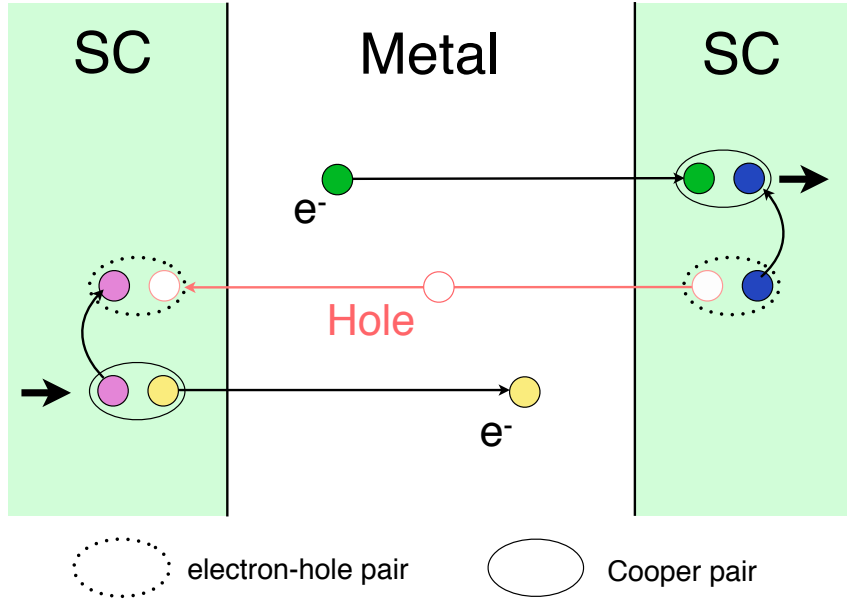


Figure 2.2: Schematic of a copper pairs tunnelling through a normal metal in a S-M-S junction. When an electron is scattered between the two superconductors it will be absorbed by the superconductors. That electron will pair with another electron emitting at the same time a hole that will break a cooper pair of the other superconductor emitting another electron to maintain time reversal symmetry. This process then will go on transporting cooper pairs from one superconductor to the other.

There is another difference between this two devices. The dc current in the dc SQUID is directly applied to the loop while in the RF SQUID the rf current is applied a circuit to which the superconducting loop in coupled as can be seen in the two schematics (Fig. 2.3).

$$\Delta\varphi + 2\pi \frac{\Phi_T}{\Phi_0} = 2\pi n \quad \text{with } n = 1, 2, \dots \quad (2.2)$$

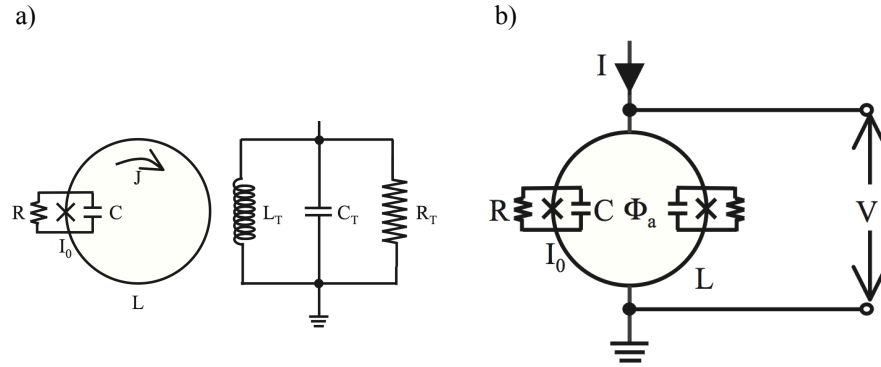


Figure 2.3: Radio frequency (rf) and dc (left and right) SQUIDs. The convention is to indicate the Josephson junctions with a X. As it can be seen the RF SQUID possesses only one Josephson junction and there is no voltage difference applied to it. Meanwhile the dc SQUID has two Josephson junctions and there is an external dc voltage applied to the SQUID. [Clarke 2006]

2.1.3 RF SQUID magnetometer

An application of the RF SQUID is as a very sensitive detector of magnetic flux. The SQUID is coupled to the LC tank circuit which is driven by a rf current. This circuit monitors the SQUID at a resonant frequency. Another element of the magnetometer is a superconductor pick-up coil that is linked to a coupling coil as seen in Fig. 2.3 a. The pick-up coil is located in a uniform magnetic field and is made out of four coils where the outer coils are wound in the opposite direction as the internal ones. This arrangement of coils creates a gradiometer which due to the coils opposite winding when a uniform field is applied the flux changes in the four coil will be equal and opposite, giving a zero net flux change. This device moves the sample inside the pick-up coils. Thus, after a careful centering of the sample, when a sample with non-zero susceptibility is moved inside the pick-up coils the flux through the coils becomes non-zero as they are no longer balanced. That difference in

magnitude between the four coils will cause a non-zero total flux change. The resulting flux change is proportional to the susceptibility of the sample. It is therefore a measure of the field gradient in the direction to the pick-up coils. The flux is transmitted to the coupling coil to the SQUID [Cukauskas 1974].

2.1.3.1 Cryogenics

For many materials the most interesting effects happen at very low temperatures. Also there are superconducting elements in the SQUID that need to be cooled down to those very low temperatures. Thus the cryogenics of the SQUID are very important. This low temperatures are achieved thanks to the of ^4He cryostat.

The sample space as well as the SQUID sensor are inside a dewar filled with liquid ^4He . The sample space is under low vacuum. This allows a good temperature diffusion. As seen in the schematic diagram in Fig. 2.4, there are two vessels through which the liquid helium gets into the cooling annulus. The gas heater heats the liquid He so it become gas and it can flow when being pumped by the vacuum pump. If a higher temperature needs to be achieved there are heaters that heat the sample space to the desired temperature. For this case we also want the flow of helium to be reduced as that flow is cooling down the temperature. The left inlet communicating the liquid helium dewar with the cooling annulus, is always open allowing flow through it while the one in the right (variable impedance inlet) can be closed by means of heating the He at the end of the inlet creating a gas bubble that prevents the liquid from passing through. There are three valves for the pump with different flow rates. The lower valve is controlled by the computer. The intermediate is an on/off valve and the top one can be regulated manually.

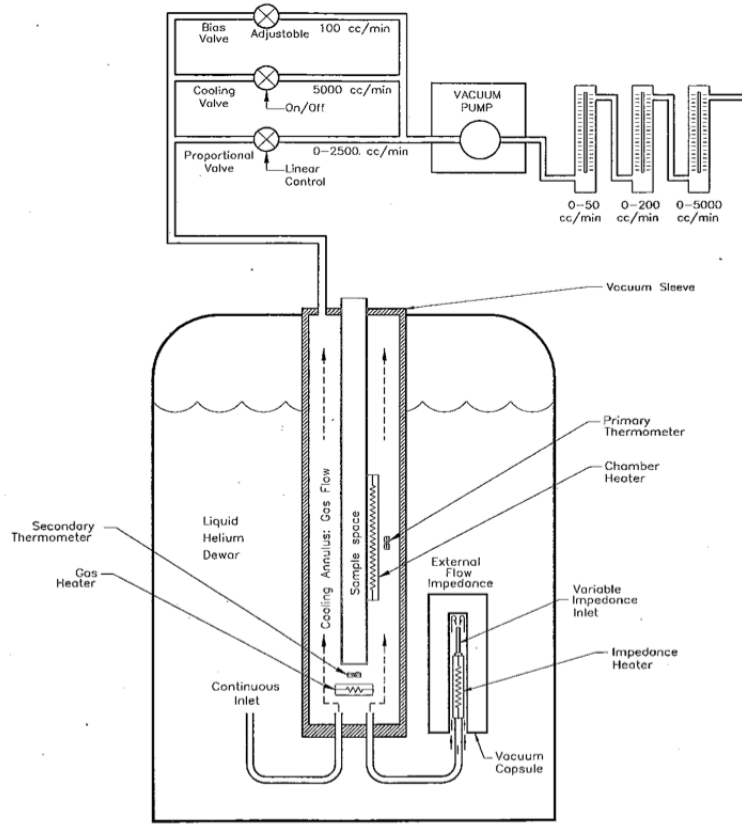


Figure 2.4: Schematics of the RF SQUID cryogenics system [Design 2013].

2.2 X-ray powder diffraction

A crystal is a periodic arrangement of atoms. The Bravais lattice is a periodic array of discrete nodes in direct space that specify the periodic distribution in which the repeated units of the crystal are arranged. Those units are called unit cells and they can contain a single atom or ion or a few, a molecule, etc [Ashcroft 1981]. Viewed from any of the units the lattice appears exactly the same. The structure of this lattice is going to be invariant under certain groups of translations and it also can be invariant under rotations. The Bravais lattice gives information about the underlying geometry of the periodic structures [Ashcroft 1981].

In the study of crystal structures, there is another lattice that has a fundamental role. This lattice is called the reciprocal lattice and is the Fourier transform of the real space lattice. Both lattices are thus related. The vectors in the reciprocal lattice are related to the planes of points in the direct lattice. If \mathbf{K} is a vector of the reciprocal lattice and \mathbf{R} is a vector of the Bravais lattice. Then, for any arbitrary vector \mathbf{r} the relation between the two lattices is given by:

$$e^{i\mathbf{K}\cdot(\mathbf{r}+\mathbf{R})} = e^{i\mathbf{K}\cdot\mathbf{r}} \quad (2.3)$$

From this relationship (2.3) we see that all reciprocal vector must satisfy the following:

$$e^{i\mathbf{K}\cdot\mathbf{R}} = 1 \quad (2.4)$$

In the Bravais lattice, different sets of planes containing the nodes of the lattice, can be defined as the parallel planes with the same spacing between them. For any set of planes in the direct space there are reciprocal lattice vectors (\mathbf{K}) perpendicular to the planes of the set. This relation between the Bravais set of planes and the reciprocal lattice vectors is very handy when specifying the orientation of the lattice planes. They represent the diffraction planes of the Bravais lattice. To identify the Bravais planes the so called Miller indices (hkl) are used. Each of the indices is a coordinate of the the shortest reciprocal vector ($h\mathbf{a}_1^*+k\mathbf{a}_2^*+l\mathbf{a}_3^*$) perpendicular to a plane (h, k, l). The Miller index is the smallest set of integers possible.

The typical interatomic distances in a crystal lattice are of the order of an angstrom. To get diffraction patterns, the wavelength of the analysing

radiation should be smaller than the interatomic distance. Thus the energy for those waves is on the order of kV which is the energy characteristic of X-rays.

X-rays can be produced in an X-ray tube, which consists of an evacuated glass envelope containing a cathode and the anode. The cathode is a filament that is heated by a low voltage so that electrons are liberated by thermionic emission. They are accelerated by the electric field due to the high voltage difference between the cathode and the anode. The target anode is typically a piece of copper that needs to be cooled down. When the high-speed electrons collide with the target they rapidly lose energy. There are two X-ray producing interactions between the incident electrons and the atoms in the target. One of these two interaction is between the incoming electrons and the electrons of the target atoms. This is the interaction that produces the X-ray used in powder diffraction analysis. If the incident electrons have certain characteristic energies, they can eject electrons from the inner orbitals of the target atoms. The vacancy left by the ejected electrons are filled by electrons from the higher orbitals. These transitions reduces the energy state of the atom by emitting X-rays with characteristic wavelengths corresponding to the difference on energy between the two orbitals. The X-ray beam due to these electron-electron interaction contains discrete energies. The other X-ray producing mechanism is by the electron-nucleus interaction. Due to the positive sign of the nucleus, the electrons slow down when they pass near an target's atom nucleus. This deceleration causes the electron to emit X-rays. But since the deceleration is not discrete but continuous the wavelength of the decelerating electrons have a wide spectrum. This spectrum of wavelength is called a white spectrum or bremsstrahlung.

The diffraction of the X-ray by the lattice planes is only going to take place when the correct geometry is achieved between the hkl set of planes, the X-ray incident angle and the position of the detector (Fig. 2.5). If the spacing between the planes from the set is d , the path difference between two X-ray rays reflected by two consecutive planes is $2d\sin(\theta)$. For the X-rays to interfere constructively the path difference must be an integral number of wavelengths

$$n\lambda = 2d\sin(\theta) \quad (2.5)$$

where n is the diffraction order; λ , is the X-ray wavelength, d is the interplanar distance of the group of diffraction planes and θ is the scattering angle. This is Bragg's condition [Cukauskas 1974]. The incident beam has to have an angle of 2θ with respect to the diffraction plane. The diffracted beam will also have an angle of θ with respect to the plane, which add a 2θ angle between the direction of the incident beam and the detector (Fig. 2.5).

To get a monochromatic of the X-ray beam, Bragg's law is used by the monochromator. For this technique only one wavelength of the full X-ray spectrum is needed. Any wavelength could be chosen but another factor to take into consideration is the intensity. Thus, just one of the most intense wavelengths of the full X-ray spectrum will be reflected by the monochromator and then collimated. This chosen wavelength is one of the electron-electron diffraction peaks. Consequently the X-ray used is the powder diffraction technique has a very defined wavelength (in the case of the X-ray apparatus used is the 1.540598 Å of copper).

Powder X-ray diffraction is based on the idea that by having the compound in powder form, all the possible planes will be available for diffraction, instead

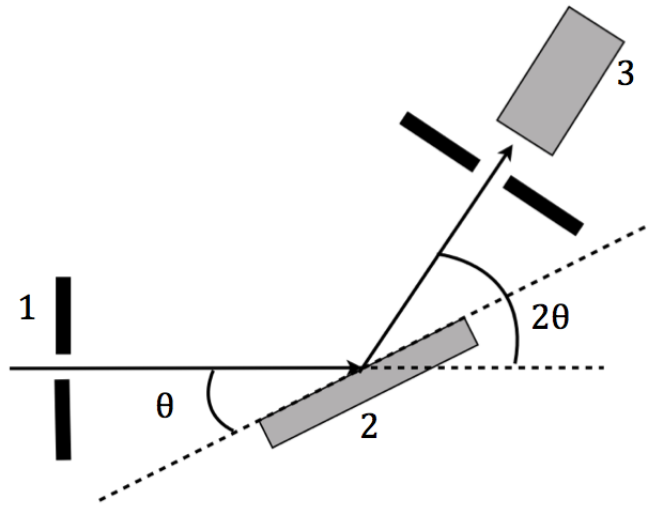


Figure 2.5: Schematic of the geometry of the X-ray diffractometer: (1) collimator, (2) powder sample mounted in the goniometer and (3) detector. The precision of angles is of the highest importance in diffraction measurements so a goniometer is used so assure that high precision.

of having to align the sample in the direction of each of the planes. The only requirement is to grind the sample down to a fine powder to ensure the presence of all possible orientations. This method is used to determine the Bravais lattice of a material and its lattice parameters.

For the powder X-ray measurements done in this work, the sample was placed on a highly polished silicon crystal wafer. The powder was held on the wafer by means of a solution of petroleum dissolved in toluene. This solution is in liquid form which allows for an even distribution. The toluene evaporates fast in contact with air. After the toluene evaporates the petroleum acts as an adhesive for the powder sample. The petroleum is invisible to the X-ray so no signature is seen in the final pattern.

Muon Spin Rotation, Relaxation and Resonance (μ SR)

Contents

| | | |
|------------|---|-----------|
| 3.1 | Principles of μSR | 27 |
| 3.2 | Zero/Longitudinal Field set up | 31 |
| 3.3 | Transverse Field geometry | 37 |

3.1 Principles of μ SR

Muon Spin Rotation, Relaxation and Resonance (μ SR) is an experimental technique that uses muons as microscopic local magnetic probes. This technique utilises the parity violation of the weak interaction to allow a study of the time evolution of muon's spin polarisation [Nagamine 2003]. As with the SQUID, this technique measures the bulk properties of a material but μ SR allows for the measuring of those properties at the local atomic level. This makes μ SR a very powerful experimental technique for the study in depth of the local internal magnetic fields directly in real-space.

Muons are a fundamental particles of nature. There are two types of muons (μ^+ and μ^-). These leptons are unstable with a mean life time of 2.2

μ s. Their charge is ± 1 and both types of muons have a spin $1/2$. The mass of this particles is roughly $1/9$ of the mass of the proton and around 207 times larger than that of the electron. As it will be seen further into this chapter, the intrinsic properties of muons and the fact that their creation and annihilation process are governed by the weak nuclear interaction, makes it possible to use them as probes to study the electromagnetic properties of matter [Sonier].

All the data presented in this thesis were taken at the TRIUMF National Laboratory, Vancouver. Negative hydrogen ions (H^-) are injected into a 6-sector isochronous cyclotron. The ions are accelerated up to energies of 500 MeV. When they reach the desired energy the hydrogen atoms are stripped of their electrons by making them pass through a thin carbon foil. After this process, the remaining nuclei have a positive charge and are consequently ejected out of the cyclotron. To create the muons for the μ SR technique the high intensity proton beam is used to create the muons in a two-step process. First the protons collide with a graphite or beryllium target [Yaouanc 2011], where pions are created via a number of nuclear reactions:

$$p + n \Rightarrow p + n + \pi^0$$

$$p + n \Rightarrow p + n + \pi^+$$

$$p + n \Rightarrow p + p + \pi^-$$

$$p + p \Rightarrow p + n + \pi^+$$

$$p + p \Rightarrow p + p + \pi^0$$

$$p + p \Rightarrow d + p + \pi^+$$

where p is a proton, n is a neutron and π^+ , π^- and π^0 stand for the three types of pions.

The second step of the muon production is when the pions decay into a muon and a neutrino as follows:

$$\pi^- \Rightarrow \mu^- + \bar{\nu}_\mu$$

$$\pi^+ \Rightarrow \mu^+ + \nu_\mu$$

where ν_μ is a muon neutrino and $\bar{\nu}_\mu$ is the antineutrino. In the experiments here presented and in general, for most μSR experiments, the muons used are positive muons μ^+ . One reason for this is that for negative muons there is a high probability for the muon to be absorbed by a positively charged nucleus due to electrostatic attraction. Usually the only pions that produce muons used in μSR are the so called surface pions. These pions are basically at rest, producing 100% polarised muons due to a maximum parity violation in the weak interaction decay of the pions. Because of conservation of linear momentum the muon and the neutrino have their moments in opposite directions. Thus the spin of the muon is antiparallel to its momentum (Fig. 3.1). As said previously, thanks to this polarisation, μSR can be used as an experimental probe.

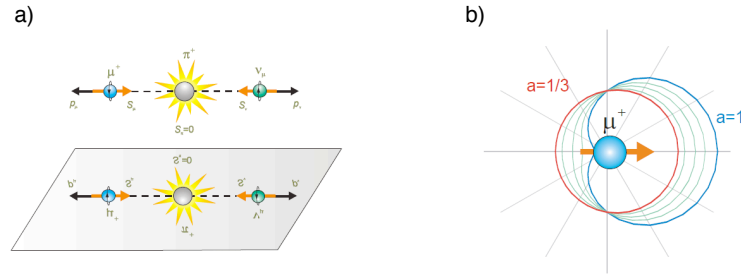
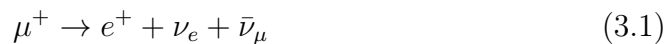


Figure 3.1: Muons production and decay is governed by the weak interaction. a) the parity violation makes the muons be emitted 100% polarised with the muon spin pointing opposite to their momenta thus conserving the linear momentum of the pion. b) when the polarised muon decays into a positron and two neutrinos the positron is emitted asymmetrically, but there is a higher probability of the positron to be emitted in the direction of the muon spin. [Sonier]

After their creation, the muons travel down the beam line to the sample

and enter the sample with the spin pointing opposite to the direction of motion. Consequently, the initial conditions of all the muons are the same. Once in the sample the muon will stop at a minimum in the electrostatic potential. For the case of positive muons landing in an ionic material, μ^+ , that will be near a negative charged ion. An important detail is that the slowing down process inside the sample does not affect the muon polarisation. Because the muon is an unstable particle, it will decay with an average lifetime of τ_μ into a positron e^+ and two neutrinos (ν_e and $\bar{\nu}_\mu$) as shown in equation 3.1. The positrons can be detected by the scintillation counter and converted into a logic pulse and registered as events occurring as function of time following their implantation. The neutrinos on the other hand won't be detected.



Since the muon decays into these particles, there is a distribution of directions from the emitted positron to travel. The angular probability distribution, $W(\theta)$, for positron to be emitted at an angle θ with respect to direction of the spin of the muon at the time of decay is given in Eq. 3.2. The asymmetry coefficient a depends on the energy of the positron. This means that a positron with maximum kinetic energy will have an asymmetry factor of $a = 1$ and the average overall energy of the positron will be $a = 1/3$ (see Fig. 3.1) [Sonier].

$$W(\theta) = 1 + a \cos(\theta) \quad (3.2)$$

TRIUMF national laboratory where the data from this work was measured is a continuous source facility where the beam has no time structure. The goal

with this type of beams is to have only one muon is inside the sample at a time. If that is not fulfilled the event will be disregarded. The continuous source accelerator allows for a very good time resolution. This resolution is needed for the measurement of high internal magnetic fields and fast relaxing signals [Sonier].

3.2 Zero/Longitudinal Field set up

To perform μ SR, there are two main experimental setup geometries: zero/longitudinal field (ZF/LF) and transverse field (TF). In the ZF/LF set up, the positron detectors are along the axis of the initial muon polarisation and a magnetic field is applied in the direction of the muon's spin (Fig. 3.2). Zero field (ZF) is very commonly used as it allows for the measurement of very small internal fields. In the case of LF the field is applied in the direction identified as the z direction which is parallel to the initial spin of the muons. The LF set up is most commonly used is by applying a longitudinal field and increasing it gradually to decouple the muon relaxation from the field distribution that the muon experiences from its surroundings. This provides information on the form of the field distribution in the sample and the measurement of T_1 relaxation.

As explained before, after the muon decays and the positron is detected, an event is registered as a positron count at a certain time. In order to get a good understanding of the physics of the sample many counts (on the order of millions) need to be acquired. With all the events, a histogram is built of the number of counts over time (Fig. 3.3). A general histogram will be modeled

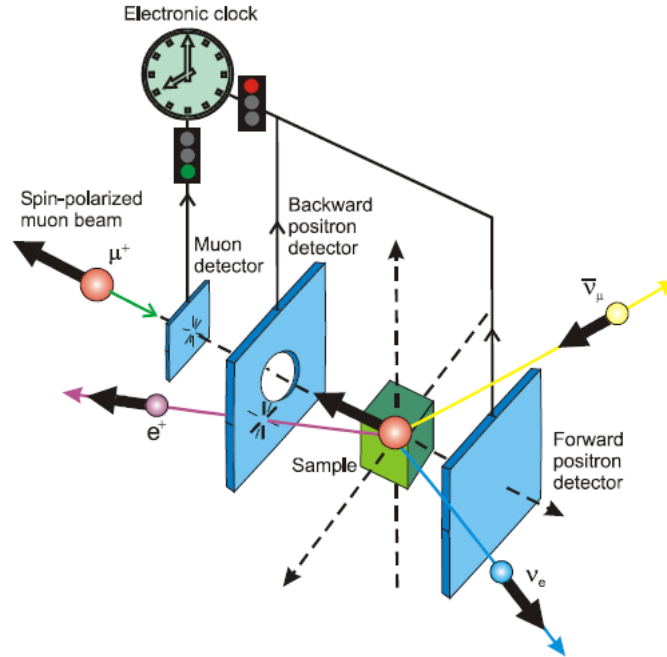


Figure 3.2: One of the experimental set ups use in μSR is the longitudinal field (LF) set up. In this experimental geometry the externally applied field is applied along the direction of the muon spin momentum. A variation of this set up is zero field (ZF) as shown in this figure. A muon enters and is detected by a scintillation detector starting a digital clock. The muon will then enter the sample an interact with the internal local field. When the muon decays only the positron will be detected by the one of the two scintillation detectors stopping the clock and creating a event at a certain time. [Sonier]

by:

$$N(t) = N_0 e^{-\frac{t}{\tau_\mu}} (1 + A_0 P_\alpha(t)) \quad (3.3)$$

where the $e^{-\frac{t}{\tau_\mu}}$ term describes the decay of the muon with its lifetime τ_μ , N_0 gives the scale, and the most meaningful physical quantity is $A_0 P_\alpha(t)$ which represents the muon asymmetry with a normalised polarisation function $P_\alpha(t)$.

From the polarisation function information about the properties of the local internal field \mathbf{B}_{loc} may be obtain. If all the muons see the same field and that field is oriented with an angle of θ with respect to the orientation

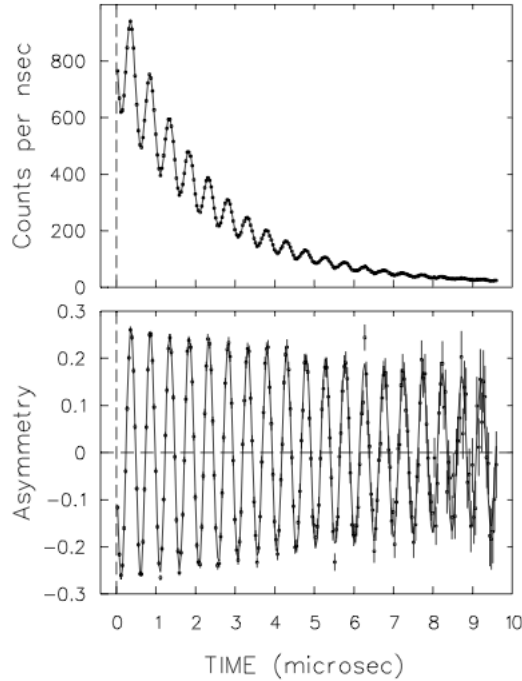


Figure 3.3: The top diagram shows a raw histogram measured from a detector from a measurement done on a sample with an internal local field. The oscillation of the signal reflect the oscillations of the muon inside the sample. The decay of the counts is due to the muon lifetime. In the asymmetry spectrum at the bottom is created by subtracting the histogram of two opposing counters and dividing it by the addition of the two same counter’s asymmetry. This gives the behaviour of the muon without the decay due to the lifetime of the muon [Kreitzman 1999]

of the spin (z direction), the spins will precess around the field as shown in figure 3.4. The precession of the spin polarisation is given by:

$$P_z(B, t) = \cos^2(\theta) + \sin^2(\theta) \cos(\omega_\mu t) \tag{3.4}$$

One of the biggest benefits of μSR is that it does not require the sample to be in single crystal form. A polycrystalline sample can be use for most experiments. This benefit comes from the fact that the ω_μ is independent of θ .

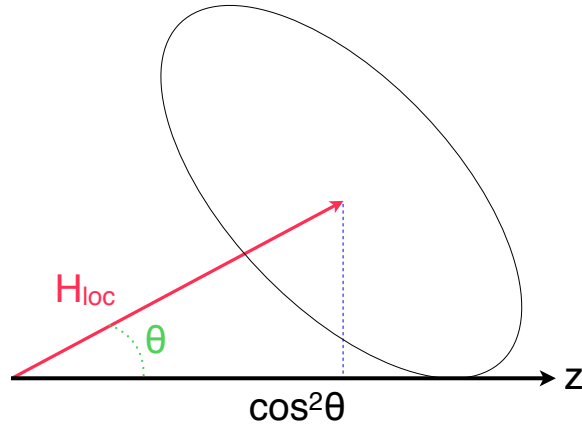


Figure 3.4: This schematic shows how the muon’s spin in this case in the z direction interacts with the local internal field \mathbf{H}_{loc} . If the angle ϑ is different from zero then the muon spin will precess around the field. Equation 3.4 defines the spin polarisation.

Because of the randomness of the polycrystalline samples there is an angular average. Thus the polarisation function 3.4, is averaged and its projection along one direction (in this case z) becomes:

$$P_z(t) = \frac{1}{3} + \frac{2}{3} \cos(\omega_\mu t). \quad (3.5)$$

At the muon stopping site the spin of the muon is going to precess with a frequency $\omega_\mu = \gamma_\mu |\mathbf{B}|$, where $\gamma_\mu = 135.538817(12)$ MHz/T is the well known gyromagnetic ratio of a muon. This relation between the frequency and the field allows for the calculation of the local static field at the muon stopping site. Plotting ω_μ vs. temperature yields the order parameter. In equation 3.5 the $1/3$ term is time independent and reflects the component of the local field along the z -axis.

So far it has been assumed that there is one unique muon stopping site with

the same value of internal local field. This indicates that the field is uniform inside the sample. However in the case that this is not realised i.e. there is some disorder in the sample that makes the field vary from stopping site to site, the oscillating part will be very quickly damped and could even disappear. This will also happen in the case that the muons precess too quickly and the oscillation will thus be averaged out because the time resolution is not good enough. For these cases the effective asymmetry above the transition, a_0 , will be damped below the transition to $a_0/3$. Many condensed matter systems have disorder due to impurities, defects or added dopants, so these last cases are very common.

If there is a distribution function of fields within a sample then the polarisation function may be obtained.

$$P_z(t) = \int \int \int P(B_x)P(B_y)P(B_z)\sigma_z dB_x dB_y dB_z \quad (3.6)$$

where it was assumed that $P(\mathbf{B}) = P(B_x)P(B_y)P(B_z)$.

In the case of a gaussian field distribution, equation 3.6 can be evaluated to give the Kubo-Toyabe (KT) function for example describes a system with a static, isotropic and gaussian random field distribution

$$P_z(t) = \frac{1}{3} + \frac{2}{3}(1 - \gamma_\mu^2 \Delta^2 t^2) e^{-\frac{\gamma_\mu^2 \Delta^2 t^2}{2}} \quad (3.7)$$

where Δ is the root-mean-square of the gaussian field distribution and gives the initial decay rate of the polarisation. The KT function exhibits a minimum at $t = \sqrt{3}/\gamma_\mu \Delta$ and then it flattens out to a value of 1/3 at long times. Polarisation functions have been evaluated for other random field distributions including the Lorentzian and incommensurate distribution, where the

polarisation function takes the form of a Bessel function [Yaouanc 2011].

The measurement begins when a muon from the collimated beam enters the sample cavity and is detected by a very thin scintillation detector. This starts a digital clock that is stopped when the positron is detected in any of the detectors. Thus an count/event is recorded as the time that the muon was inside and in which of the detectors was the positron measured. As mentioned before a histogram is built that allows for the spatial and temporal resolution of the fields inside the sample [Yaouanc 2011].

The most common way to analyse μSR data is to use the asymmetry of a pair of opposing detectors. The combination can be either backward (B)-forwards (F) counters in the direction of the beam or up (U)-down (D) or left (L)-right (R) counters. Using the two counter's histograms (equ. 3.3), the experimental asymmetry $A(t)$ (see bottom graph of figure 3.3) is defined as:

$$A(t) \equiv \frac{N_F(t) - N_B(t)}{N_F(t) + N_B(t)} = \frac{(1 - \alpha) + (1 + \alpha\beta)A_B G_z(t)}{(1 + \alpha) + (1 - \alpha\beta)A_B G_z(t)} \quad (3.8)$$

where the following normalisation parameter have been defined:

$$\alpha \equiv \frac{N_{0F}}{N_{0B}} \quad (3.9)$$

$$\beta \equiv \frac{A_{0F}}{A_{0B}} \quad (3.10)$$

Generally $\beta \sim 1$ and α is obtained from calibration spectra

3.3 Transverse Field geometry

In this geometry an external dc magnetic field H_0 is applied to the sample perpendicular to the initial direction of the muon spin as seen in figure 3.5. When the muons are implanted in the sample they start precessing in the external applied magnetic field. The total local field B_{total} seen by the muons is the vector sum of the local field B_{loc} plus the externally applied field $B_{applied}$.

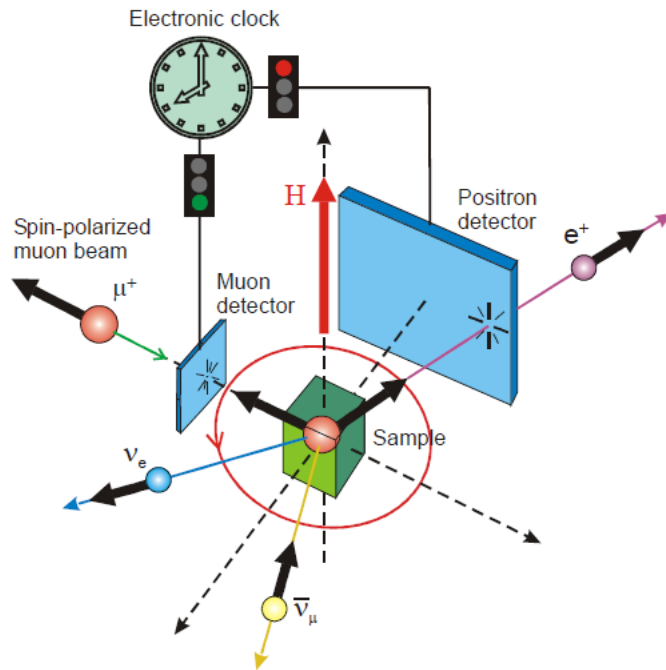


Figure 3.5: In the transversed field (TF) set up and external field is applied perpendicular to the muon spin polarisation direction. The muon is detected as it enters the sample by a thin muon detector that starts the digital clock that will be stop when the positron is detected after it is created from the muon decay. For this experimental configuration the two most used pair of detectors are the up or down and left and right. [Sonier]

This setup is commonly use to measure Knight shifts or frequency shifts, the investigation of phase separation in magnetic systems and the determination of the physical properties of field distributions in matter. The Knight

shift is a great tool to measure the local magnetic susceptibility by the comparison of the measured frequency with the frequency of the applied external field. In the case of the type II superconductors the transverse field set up is employed to measure the field distributions from flux vortices and determined the penetration depth and coherence length.

In transverse field the external field is usually applied in the direction of the muons' momentum (z direction) as seen in figure 3.6. Unless the field is applied in the same direction of the beam momentum the muons would miss the sample. Thus to achieve the transverse field setting the muon's spin is rotated 90° . This is called the spin rotated mode. The momentum is still in the z direction but the spin is now in the x or y direction. The separators work by applying very strong magnetic field perpendicular to the beam (x or y direction) which make the spin of the muon start rotating around the magnetic field. However, the application of that magnetic field would make the momentum of the muon rotate as dictated by the Lorentz force. To avoid the rotation of the muon's momentum, an electric field is applied in the y or x direction that exerts a force equal but in opposite direction to the Lorentz force. This keeps the muon momentum in a straight path as well as it removes positron contamination from the beam. Accordingly, the muons are inside the separators long enough to have their spins rotated 90° in the y - z plane.

The presence of a static internal field distribution in a TF experiment causes dephasing of the muon spin ensemble [Yaouanc 2011]. In this setup the important polarisation is $P_x(t)$ along the x direction instead of the polarisation along the z direction for the ZF case. The $P_x(t)$ is used to study the field distribution along the z direction which is the one along which the external field B_{ext} is applied. For the simplest case of a gaussian field distribution,

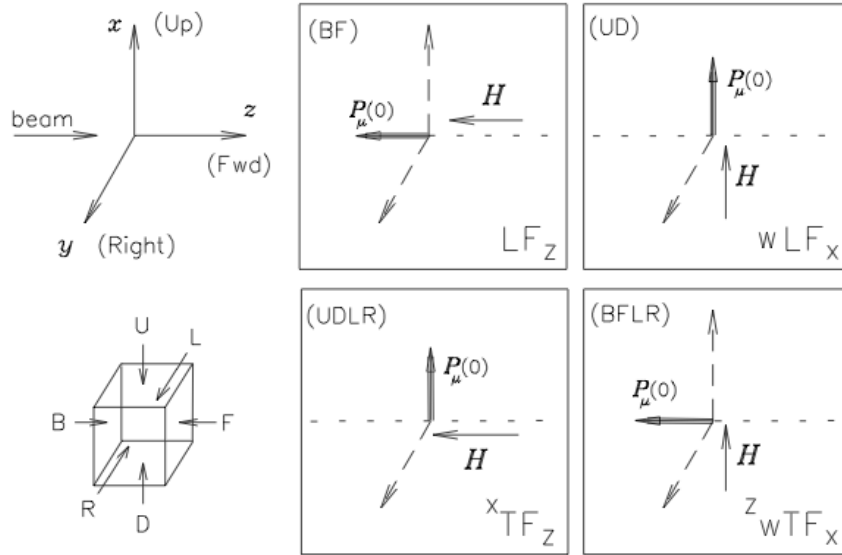


Figure 3.6: Schematics of the coordinate system and labelling used in μSR . The beam will always be in the z direction. In both the longitudinal field (and zero field) as well as the weak transversed field the muon's spins point in the z direction while for the transfers field the spins are rotated to point x direction. [Kreitzman 1999]

the resulting polarisation will be given by a gaussian envelope multiplied by a cosine function:

$$P_x(t) = \exp\left(-\frac{\gamma_\mu^2 \Delta^2 t^2}{2}\right) \cos(\omega_\mu t) \quad (3.11)$$

where $\omega_\mu = \gamma_\mu B_{ext}$.

In the case that the internal field distribution is not static the most straight forward way to parametrised that dynamics is by the definition of a single magnetic correlation frequency ν_c . Furthermore in the extreme limit when the dynamics is fast ($\nu_c \gg 1$) the envelope becomes exponential:

$$P_x(t) = \exp(-\lambda_X t) \cos(\omega_\mu t) \quad (3.12)$$

were $\lambda_X = \gamma_\mu^2 \Delta^2 / \nu_c$. This is the polarisation equation used to fit ZF asymmetry spectra in this study (see chapter 4).

Weak transverse field (wTF) is a special case of the transverse field set up. The field is also perpendicular to the spin of the muon but due to the fact that the fields are smaller than the ones used in TF there is no need to rotate the spin of the muons. Thus the field is applied in the x or y directions and the muon's spin remains in the z direction. This type of measurement is often used to determine the value of α from equation 3.8 for the present detector settings. It also can be used, as it was used for this work, to measure the paramagnetic volume fraction of a sample using the same polarisation described for the TF set up. When the weak transverse field is applied, if the sample is ordered the internal local field will be much bigger than the externally applied field. Thus if the precision frequency measured is the same as the field applied the system is not ordered and is paramagnetic. There is also a wTF-wipeout that is the loss of asymmetry in the ordered volume fraction. This occurs when the internal field is larger or comparable to the applied field as the

Results

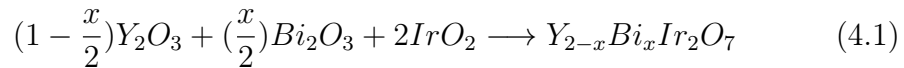
Contents

| | |
|---|-----------|
| 4.1 Susceptibility | 42 |
| 4.1.1 FC and ZFC at 1T | 42 |
| 4.1.2 FC at 100G | 46 |
| 4.2 X-ray Analysis and Rietveld refinement | 47 |

In this thesis the attention has been focused on the study on the magnetic properties of the very interesting family of pyrochlores $Y_{2-x}Bi_xIr_2O_7$. The magnetic properties have been studied using a DC SQUID magnetometer and muon spin rotation, relaxation and resonance (μSR). The results from this study are presented and analysed in this chapter. Other groups [Yanagishima 2001] [Soda 2003] [Aito 2003] have analyzed the electrical transport of this system. For the electrical resistivity they all report a metal insulator transition that disappears above a bismuth doping of $x \sim 0.5$ (25%). These publications also show that the MI transition is doping dependent and that the MI transition occurs along with a magnetic transition, thus it is connected with the magnetic behaviour of the Ir.

The samples analyzed in this work analysed are: the pure sample of $Y_2Ir_2O_7$ and the doped samples of $Y_{2-x}Bi_xIr_2O_7$ with doping: $x = 0.2$, two

0.4 samples to check sample dependence, 0.9 and 1.3 as well as the fully doped $\text{Bi}_2\text{Ir}_2\text{O}_7$ sample. These are all polycrystalline samples and were prepared by the Ian Fisher group at Stanford University. They were created by stoichiometrically adding molar ratios of IrO_2 , Y_2O_3 or Bi_2O_3 with purities of 99.99% as follows:



After pelletizing, the mixture underwent a series of annealings at 1000° in air with intermediate grindings. The annealing times varied from 150 hours to 600 hours.

4.1 Susceptibility

The *DC* magnetization of the four samples were measured using a SQUID magnetometer at McMaster University as described in Chapter 2. The susceptibility measurements were done to have a first overall characterisation of the materials. This allowed the understanding of the general behaviour of the $\text{Y}_{2-x}\text{Bi}_x\text{Ir}_2\text{O}_7$ samples and to help in the analysis and fitting of the μSR data. This results also gave a first sense of the quality of the samples.

4.1.1 FC and ZFC at 1T

The polycrystalline samples were loaded into the SQUID in gel capsules and the same sequence with a 1T field was run for all the samples to measure the susceptibility. As part of the data processing the magnetisation was divided by the field to obtain the susceptibility of the sample. As said in the introduction chapter (Chap. 1) the only ion with a magnetic moment is the iridium. Thus

| Element | Molar mass (g/mol) |
|---------|--------------------|
| Ir | 192.217 |
| Bi | 208.98 |
| Y | 88.905 |
| O | 15.999 |

Table 4.1: Molar masses values used in this work for the calculation of the susceptibility per mol of iridium using equation 4.2.

it is more interesting to find the susceptibility per mol of iridium. This was calculated by dividing the susceptibility by equation 4.2 (using the values of the molar masses in table 4.1).

$$2 \frac{\text{mass of the sample (g)}}{\text{molar mass of sample (g/mol)}} \quad (4.2)$$

$$\text{molar mass of sample} = (2-x)Y + xBi + 2Ir + 7O = x(Bi - Y) + 2Y + 2Ir + 7O$$

From the analysis of the data, it can be seen that there are some interesting features in the susceptibility (Fig. 4.1). Two of the most prominent features are: first, the difference between the zero field cooled (ZFC) signal and the field cooled (FC) signal and second, the transition temperature marked by the departure of the signals from each other. The increase of the susceptibility after the transition indicates that the system undergoes a bulk phase transition to an ordered state. This transition to an ordered state is absent on the fully doped $\text{Bi}_2\text{Ir}_2\text{O}_7$. The reasons that this occurs will be discussed later on in the chapter. Meanwhile, the low ZFC susceptibility shows that the spins have been locked or frozen into a state and there is an energy barrier to unlock them. Despite the strong external applied field of 1T the spins do not align with the field in the ZFC, meaning that the energy barrier is relatively strong. On the contrary, if the system is cooled down with a field applied, the spins

can align with the external field. The FC state is a weak ferromagnetic state. The small magnetic moment exhibited by the samples and the shape of the magnetic transition are reminiscent of a spin-glass-like transition but it could also be attributed to a canted antiferromagnetic state. This behaviour is more pronounced in the pure and less doped samples and decreases with doping.

Bismuth is non-magnetic. The action of substituting the $\text{Y}_2\text{Ir}_2\text{O}_7$ pyrochlore with this non magnetic atom decreases the susceptibility of the system as well as the transition temperature: $T_N \sim 145$ K for $x = 0.2$, $T_N \sim 75$ K for $x = 1.3$ and no transition for the $\text{Bi}_2\text{Ir}_2\text{O}_7$ (Fig. 4.1). In addition, the difference between FC and ZFC decreases as doping increases. So that at $x = 1.3$ the FC and ZFC signals are almost indistinguishable and for the fully doped sample there is no difference. At lower temperatures ($T \lesssim 10$ K) there is another feature where the susceptibility increases with decreasing temperature. This additional increase of the susceptibility is likely to be due to weak paramagnetic impurities as μSR measurements in chapter 5 will show the absence of an extra magnetic phase.

One explanation of the behaviour seen in the susceptibility could be the difference in the electron orbitals of the different ionic radii. This difference affects the electronic interactions and exchange introducing disorder as the yttrium is substituted. In addition, there is evidence of Bi off-centering in metallic iridium pyrochlore [Shoemaker 2011] that would explain the destruction of magnetic order. So at the higher levels of doping the physics of the system is supposed to change to a metallic state without a magnetic transition to an ordered state. Just by using the SQUID magnetometer can not tell how the impurities have been accepted into the system. A local probe is needed for that type of study. However the effect of the substitution can be

still be seen in many features of the susceptibility of this system.

| | Yttrium +3 | Bismuth +3 |
|------------------------|------------|-----------------------------|
| ionic radii (Å) | 1.02 | 1.17 |
| electron configuration | [Kr] | [Xe] $6s^2 4f^{14} 5d^{10}$ |

Table 4.2: Ionic radii values reported for iridium and bismuth [Shannon 1976] and electronic configuration.

As the doping is increased the behaviour of the samples does not follow an obvious progression. The FC signal for $x = 0.9$ is higher than the signal both $x = 0.4$ and very similar again to $x = 0.2$. The more natural progression would have been that the susceptibility would have decreased with doping. This would mean smaller and smaller signal as the doping is increased. However, this behaviour is not what is seen in the susceptibility measurements. As will be seen further into the chapter, the reason is that there is a synthesis problem with the 0.9 and 1.3 samples.

| x | T_N (± 5 K) | T_{max} (± 5 K) |
|---------|--------------------|------------------------|
| 0 | 162.5 | 158.5 |
| 0.2 | 149.0 | 133.5 |
| 0.4 | 142.5 | - |
| 0.4 (2) | 146 | - |
| 0.9 | 126.0 | 110 |
| 1.3 | 91.0 | - |
| 2 | 0 | 0 |

Table 4.3: List of the Neel temperature T_N for all the samples. As well is shown the temperature at which a maximum in the ZFC susceptibility is register for some of the samples.

The susceptibility (Fig. 4.1) at high temperatures for all the concentrations shows an almost temperature independent behaviour. When plotting the inverse of the susceptibility (Fig. 4.2), the Néel temperature calculated

for the four samples is very large (~ -1500 K). This big difference between the Néel temperature and the transition temperature and the fact that the $\text{Y}_{2-x}\text{Bi}_x\text{Ir}_2\text{O}_7$ material orders in a pyrochlore structure suggests that there is magnetic frustration at low temperatures. Magnetic frustration is very common in pyrochlores and it will have an effect on the magnetic order of the sample only allowing the spins to arrange in a certain way (chap. 1).

4.1.2 FC at 100G

To check the consistency of the results, a measurement of the susceptibility was carried out for all the dopings (0.2, 0.4, 0.9 and 1.3) with an applied field of 100G and compared to the previous 1T data (Fig. 4.3). In this case only a field cooled measurement was carried out. Again, an increase of the susceptibility is seen in the 100G data below the transition temperature. In this new field there is no ZFC data but it can be seen that the transition temperature appears to change. It can also be seen that the susceptibility decreases with field both above and below the transition temperature. At high temperatures Shapiro and co-workers showed in their paper [Shapiro 2012] that the susceptibility is field independent. Such behaviour has not been seen in the results presented in this work. The meaning of this difference in results is still not well understood. Again, there is a strange progression of the susceptibility as bismuth is substituted by yttrium in the field comparison. The $x = 0.9$ signal is larger than the $x = 0.4$ and similar to the $x = 0.2$ but shifted.

After the evidence of irregular behaviour from the samples, the next step was to do X-ray Rietveld refinement to find the cause of this interesting behaviour.

4.2 X-ray Analysis and Rietveld refinement

X-ray Analysis and Rietveld refinement was done to better characterise the samples. Hence by looking at how the lattice parameter changes the changes of the structure can be monitored.

For the purpose of the refinement, X-ray power diffraction scans were taken for each of the samples. The 110° full scans were done at room temperature using the Panalytical machine described in chapter 2. The data was analysed using the FULLPROF SUITE. The $\text{Y}_2\text{Ir}_2\text{O}_7$ structure reported by Shapiro *et al.* [Shapiro 2012] was used as the starting structure with cubic space group Fd-3m. Variables in the refinement included: the lattice parameters, the anisotropic thermal parameters and oxygen O1 x fractional coordinate. Pseudo Voigt was the function used in this refinement. The cubic lattice constant was refined for all the samples and their values can be seen as a comparison with published data in Fig. 4.4.

For two of the samples ($\text{Y}_2\text{Ir}_2\text{O}_7$ and the second sample of $\text{Y}_{1.6}\text{Bi}_{0.4}\text{Ir}_2\text{O}_7$), a standard of Si was added to the scan to ensure of the correct alignment of the Panalytical x-ray machine but the Si peaks were then excluded for a better refinement of the main phase. The green asterisks in Fig. 4.5 mark the position of the silicon peaks.

As Aito and co-workers show in their paper (Fig. 4.4), the increase of the lattice parameter as the doping of bismuth increases is expected to be linear, if the impurities are accepted into the lattice following Vegard's law. This empirical law states that at a constant temperature there is a linear relation between the lattice parameter and the amount of the doping elements (red line in Fig. 4.4). Some of the results in this work obtained do not follow

| Targeted x | Measured x | Bi targeted percentage | Bi measured percentage |
|--------------|--------------|------------------------|------------------------|
| 0.9 | 0.29 | 45 | 14.5 |
| 1.3 | 0.41 | 65 | 20.5 |

Table 4.4: The amount of bismuth in the high doped samples calculated from Fig. 4.4 is different from the targeted.

this expected behaviour. On the contrary, the high doping samples used for this work, ($x = 0.9$ and 1.3) have a much smaller lattice parameter than that expected from the Vegard's law. The error bars of the calculated parameters are not big enough to account for the difference between these points and the Aito *et al.* values. With the help of the guide to the eyes in Fig. 4.4 it can be seen that the real doping for the higher dopings can be estimated (see table 4.4).

One explanation for the difference of the lattice parameters can be that the initial products were not fully reacted. If that is the case, only a certain amount of the precursors reacted and the rest were left as extra phases. To test this theory, a pattern comparison between the x-ray diffraction data and a calculated pattern from the database was carried out. The reason why the comparison is necessary is because the refinement will only give the lattice parameters of the impurities which makes it hard to identify those impurities just by the lattice parameter. The comparison technique overlays the database patterns on top of the diffraction data. Then a simple comparison of two, gives the exact composition of the peaks in the case that both match. This analysis is done on the XRD Software - DIFFRAC.EVA program by Bruker.

When comparing the database pattern with the measured pattern it can be seen which peaks do not correspond to the desired phase and which are indicative of secondary phases. In the comparison of the pure $\text{Y}_2\text{Ir}_2\text{O}_7$ and

the $x = 0.2$ and $x = 0.4$ samples a small percentage of remnants of unreacted Y_2O_3 and IrO_2 phases can be seen, specially the iridium oxide which is the magnetic phase. Having remnants of a magnetic phase is not very desirable as they can change and influence the magnetic properties and behaviour of the main phase. In this case the contamination is small so it does not cause a big problem. On the other hand the $x = 0.9$ and $x = 1.3$ samples show evidence of significant amounts of the precursor phases as well as some unidentified phases. The presence of these secondary phases in relative large amounts contributes to the strange signal on the susceptibility and thus disqualified them for future measurements. Collaborators at Stanford University have worked very hard to produce new good quality samples of the $x = 0.9$ and $x = 1.3$, process that has taken over several months. These new samples will shortly be analysed.

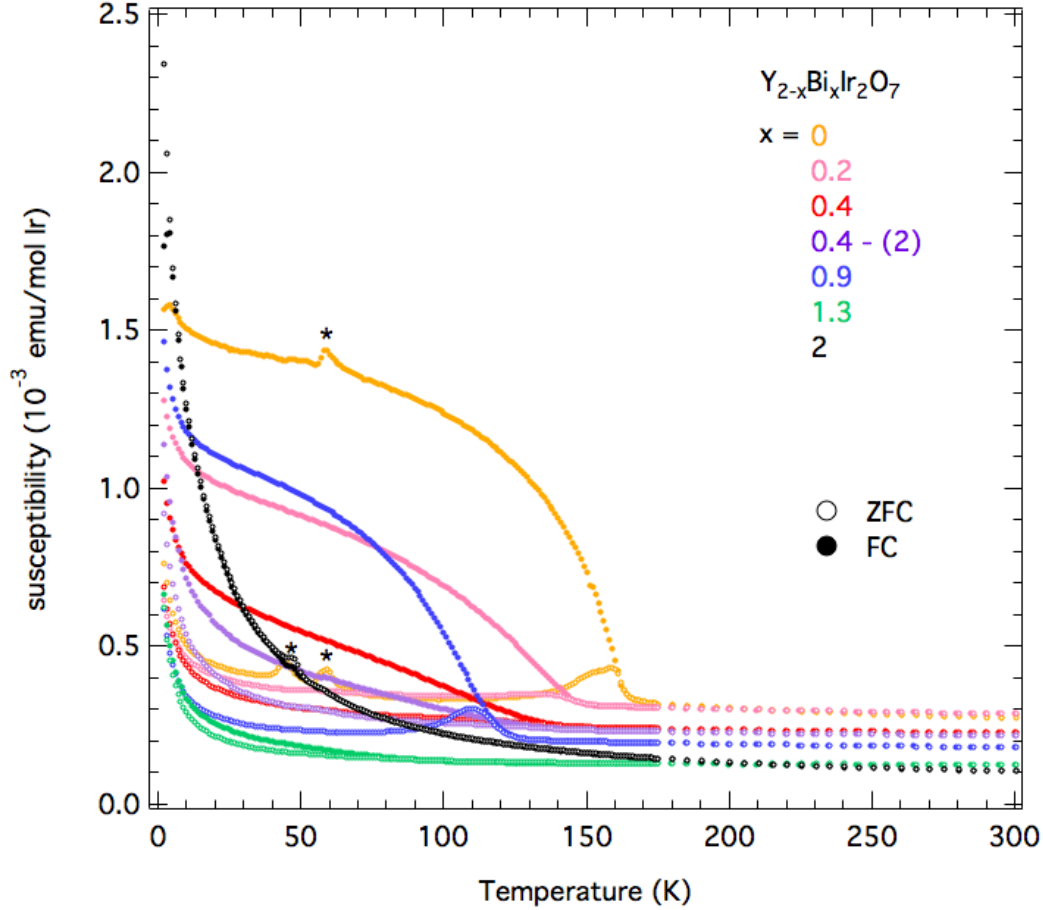


Figure 4.1: Magnetic susceptibility on the powder samples $Y_{2-x}Bi_xIr_2O_7$ $x = 0, 0.2, 0.4, 0.4-(2), 0.9, 1.3$ and 2 in a 1 T field. A zero field cooled (ZFC) and a field cooled (FC) measurement was done for every sample. The departure of the ZFC and ZF signals marks the transition to an magnetically ordered state (see table 4.3). This difference shows a small magnetic moment due to a weak ferromagnetic order which is in agreement with the picture of canted antiferromagnetic order. The $Bi_2Ir_2O_7$ sample does not have a transition as the ZFC and FC signals do not depart from each other. When carrying the measurement on the SQUID magnetometer each point is measured over a small amount of time (~ 2 minutes). This amount of time allows to the spins to align with the external field even in ZFC run. This created the small peak seen for $x = 0.2$ and 0.9 samples at 140 K and 110 K respectively. The peaks mark with an asterisk (*) correspond to oxygen peaks trapped in the sample cavity at the time of the measurement.

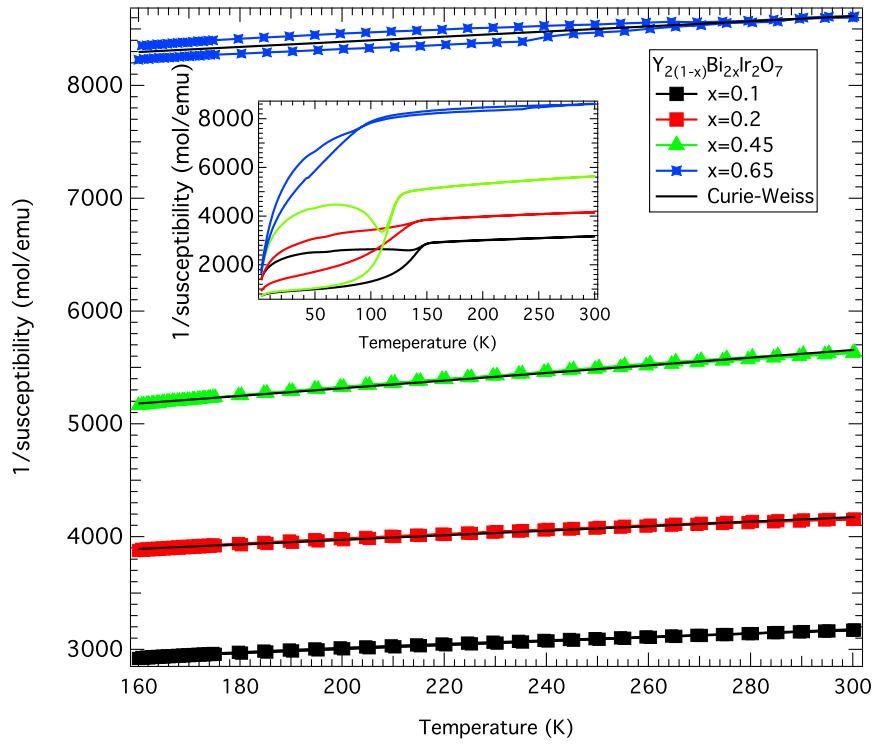


Figure 4.2: Inverse of the susceptibility from the 1 tesla measurements shown in Fig.4.1. A Curie-Weiss (black line) law has been fitted to find the Néel temperature of the four samples. The inverse of the susceptibility of the whole temperature is plotted in the inset.

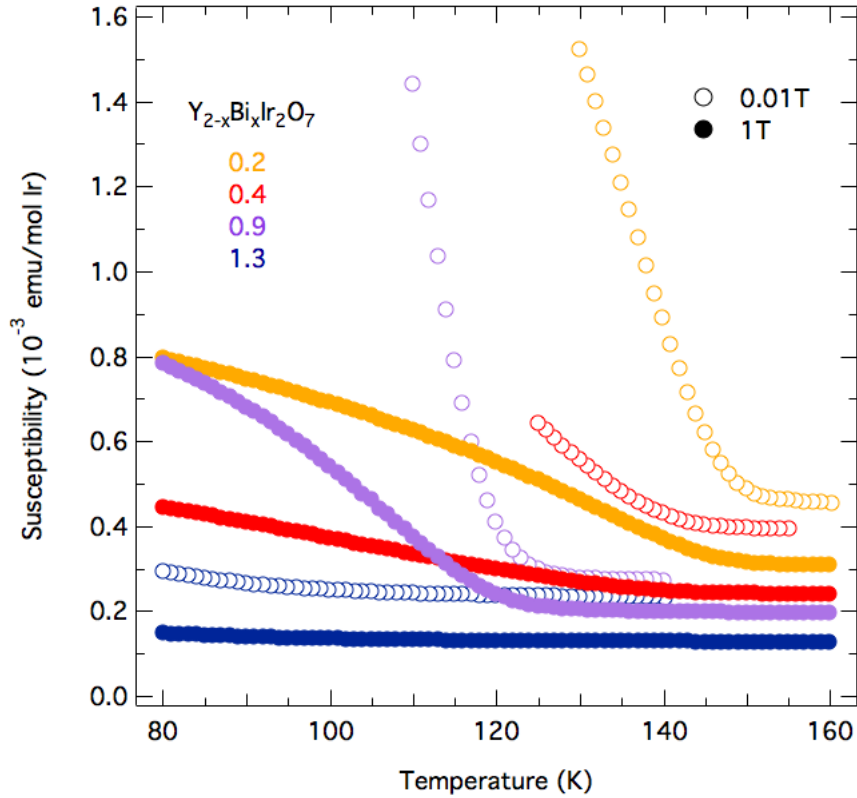


Figure 4.3: Comparison of the field cooled magnetic susceptibility at 100 G (full circle) and 10000 G (empty circle) applied field vs. temperature on the transition temperature regime on the doped samples $x = 0.2, 0.4, 0.9$ and 1.3 . There seems to be a change to the transition temperature with field for some samples. But it can be seen that there is a decrease in the susceptibility with increasing field.

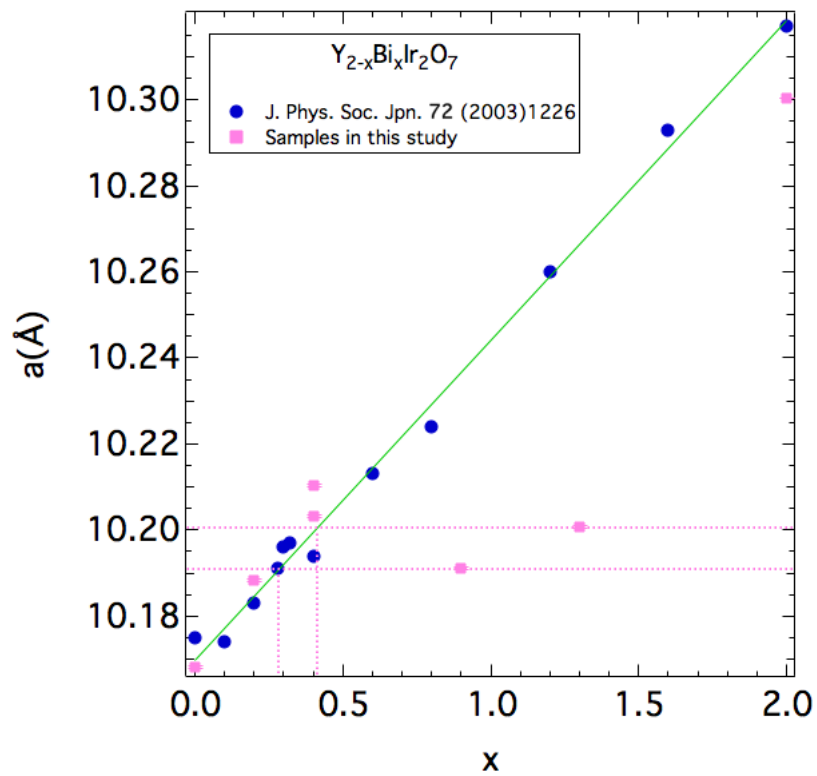


Figure 4.4: The X-ray refinement shows that the higher doped samples did not have the desired amount of bismuth. The total amount of bismuth was not fully accepted by the pyrochlore lattice and thus the lattice parameter was smaller than expected. In this figure the actual amount of bismuth can be approximated by extending lines (dotted lines) to the fit line (solid line).

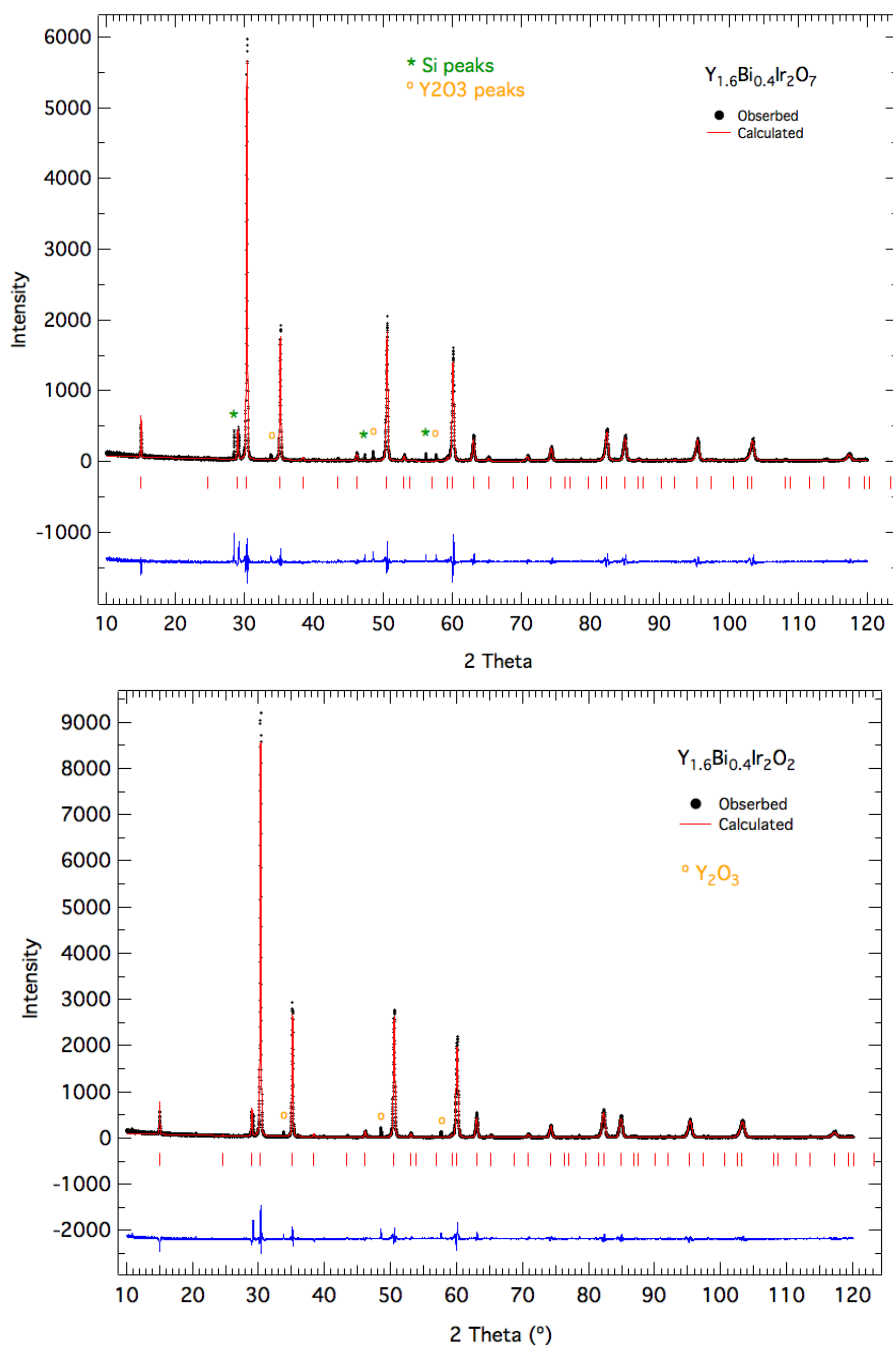


Figure 4.5: Powder-diffraction data (circle) of the two $x = 0.4$ samples measured at room temperature. The red solid line shows the Rietveld refinement and with the blue solid line it can be seen the difference between the observed and the calculated refinement. The vertical sticks show the position of the peaks. Both refinement shows that the results are consistent. In both cases there is a small amount of unreacted Y_2O_3 which peaks are indicated with the yellow circle. For one of the samples a silicon standard (green star) was added to check the correct alignment of the diffractometer.

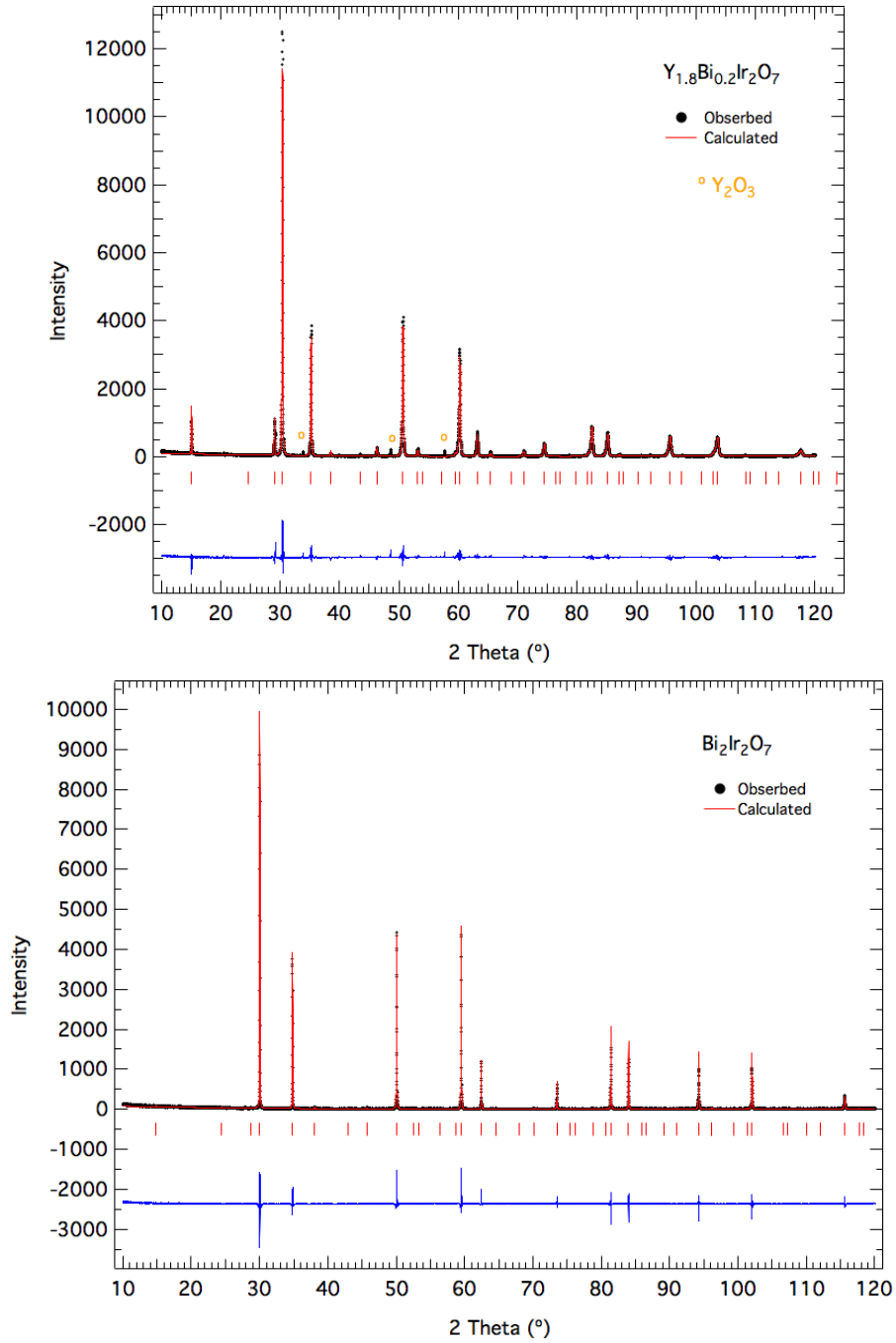


Figure 4.6: Powder-diffraction data (circle) of the $x = 0.2$ (top) and fully doped $Bi_2Ir_2O_7$ (bottom) measured at room temperature. The red solid line shows the Rietveld refinement and the blue solid line shows the difference between the observed and the calculated refinement. The vertical sticks show the position of the peaks. The $Bi_2Ir_2O_7$ sample has no sign of secondary phases showing a great quality sample. Meanwhile the $Y_2Ir_2O_7$ and $Y_{1.8}Bi_{0.2}Ir_2O_7$ samples have some yttrium oxide unreacted left in them indicated by the yellow circles.

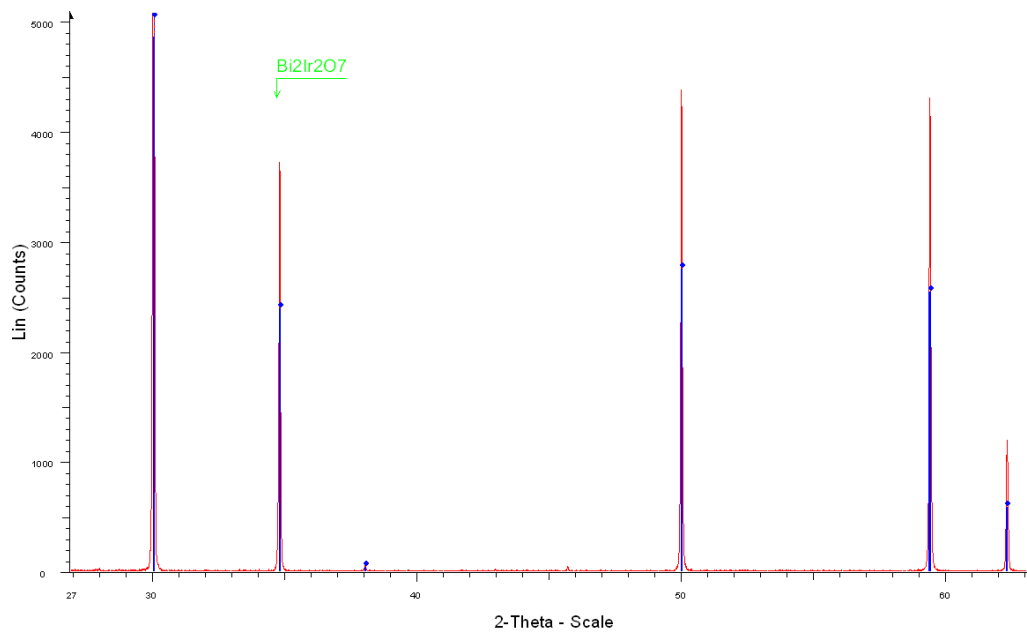


Figure 4.7: The powder-diffraction data of the Bi₂Ir₂O₇ is here compared with a database calculated pattern showing a great agreement between the two. There is no evidence of any secondary magnetic phases.

μ SR results

Contents

| | | |
|------------|--|-----------|
| 5.1 | $Y_{2-x}Bi_xIr_2O_7$ results | 57 |
| 5.1.1 | Zero field | 58 |
| 5.1.2 | Weak transverse field and transversed field | 62 |
| 5.2 | $Bi_2Ir_2O_7$ results | 64 |

5.1 $Y_{2-x}Bi_xIr_2O_7$ results

μ SR measurements were done at TRIUMF, UBC at the M15 beamline with a 4He cryostat on pure $Y_2Ir_2O_7$ and doped samples ($x = 0.2, 0.4, 0.9$ and 1.3). The fully doped sample of $Bi_2Ir_2O_7$ was measured using a dilution refrigerator (DR) on the same beam line. All the samples were in polycrystalline form. The $Bi_2Ir_2O_7$ sample was made into a pellet of 2.5 cm in diameter and ~ 1 mm in thickness pellet and cintered at 1000° for 24h in air. This process of pelletizing and annealing had to be done to ensure good thermal contact in the dilution fridge (DR) cryostat use for these measurements. The analysis of the data was done using the MSRFIT program.

5.1.1 Zero field

Using the zero field (ZF) set up it is possible to measure the internal fields at the muon stopping site (for more details refer to chapter 3). Each sample was measured in this setup over a wide temperature range $2\text{K} < T < 200\text{K}$.

To be able to extract all the information from the samples, the asymmetry curves need to be fitted. In this case they were fitted using a depolarisation function appropriate for a magnetically ordered polycrystal. Fig. 5.1 (b), shows at low temperatures a first fast relaxation, followed by a short period of oscillations and a long relaxation to zero for the asymmetry curves of the $x = 0.2$ sample. For this reason three different signals were added together to form the fitting function:

$$P(t) = A_1 \exp(-\lambda_1 t) \cos(\omega_\mu t + \phi) + A_2 \exp(-\lambda_2 t) + A_3 \exp(-\lambda_3 t) \quad (5.1)$$

Below the transition temperature, the asymmetry plots (Fig. 5.1 (b)), show for the pure and $x = 0.2$ samples that there are oscillations indicating spontaneous muon precession. As the oscillations are well defined, it can be deduce that there is commensurate order with a magnetically unique muon stopping site. That is, there is an homogeneous and static internal magnetic field below the transition temperature. The oscillations of the pure material below the transition temperature were already observed with μSR by Disseler *et al.* [Disseler 2012]. The order seen at low temperatures is suppressed by increasing the doping and by increasing the temperature above the transition temperature. Above the transition temperature (Fig. 5.1 (a)), there are no oscillations as the samples have become paramagnetic and thus there is no

unique local non-zero internal field at the muon stopping site. For higher doped samples the amplitude of the oscillation is very rapidly reduced until it disappears by $x = 0.4$. However, it is very interesting to see that the frequency of the oscillations at the lowest temperature does not vary when adding bismuth (Fig.5.2).

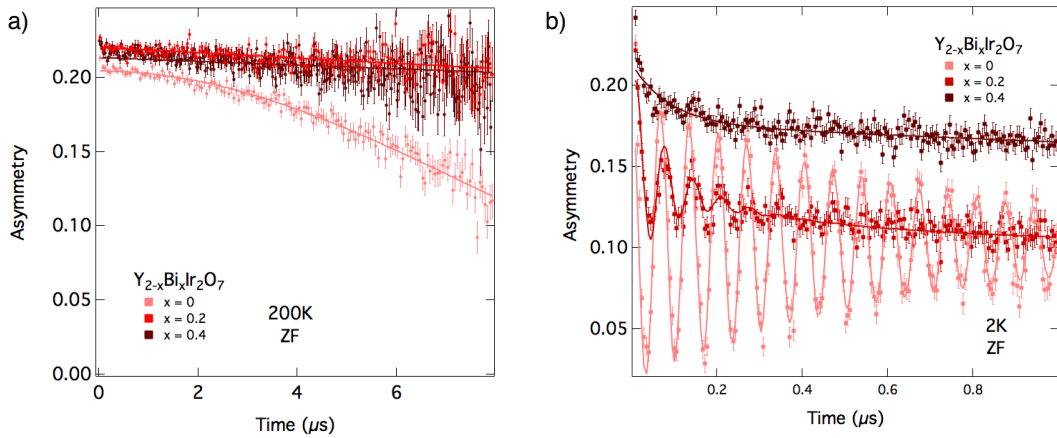


Figure 5.1: (Colour lines) Zero field μSR data with fits to Eq. 5.1 of the pure $Y_2Ir_2O_7$ and the doped sample $x = 0.2$. (a) shows the behaviour of both samples above the transition temperature (200 K) where no sign of magnetic is observed as expected in the paramagnetic regime. (b) Below the transition temperature (2 K) the oscillation observed in both samples indicates the presence of internal magnetic field. For the low temperature graph only the first microsecond was plotted with the purpose of making the oscillations more clear to the eye. This two samples are the only ones that show evidence of internal magnetic field below the transition temperature.

By plotting the frequency (ω_μ) as a function of temperature, the magnetic order parameter can be obtained (Fig. 5.2). The frequency is temperature dependent and the onset of the muon precession gives the transition temperature (table 5.1). The frequency increases monotonically as temperature is lowered following a phenomenological mean-field equation $\langle B_{loc} \rangle \sim [1 - (T/T_c)^\alpha]^\beta$. At

| x | χ T _N (K) | μSR ZF T _N (K) |
|-----------|---------------------------|--------------------------------|
| 0 | 162.5 | 160 |
| 0.2 | 149.0 | 130 |
| 0.4 | 142.5 | - |
| 0.4 - (2) | 146 | - |

Table 5.1: List of transition temperatures extracted from two different measurements on the same sample. There is a slight discrepancy between the two temperatures.

low temperatures the frequency reaches a maximum value $\omega_\mu = 14.967(6)$ MHz at 2 K for the $Y_2Ir_2O_7$ and $\omega_\mu = 15.0(3)$ MHz at 2 K for $x = 0.2$. From these values the local internal magnetic field can be calculated using the frequency and field relation discussed in chapter 3; $\langle B_{loc} \rangle = \omega_\mu / \gamma_\mu = 1104.6$ G for the pure iridium iridate and $\langle B_{loc} \rangle = 1107.011(2)$ G for $x = 0.2$ sample. The fact that the frequency, and hence the internal field stays the same as the bismuth is increase has very strong implication when defining the effect of the Bismuth to the magnetic order of the sample in the ordered state. When adding bismuth, the magnetic field due to the iridium ions stays the same but the non-magnetic regions of the part get bigger and bigger, thus decreasing the amplitude. This means that the Bi substitution does not initially destroy the order completely but does destroy the long range order.

The decrease of the transition temperature and the constant frequency could be due to the chemical pressure from the different ionic radii of the two ions. This could affect the bond lengths and angles which could alter the magnetic exchange between the Ir moments. The possibility of having big clusters of $Bi_2Ir_2O_7$ and $Y_2Ir_2O_7$ was discarded from the X-ray results as no such phases were seen in the X-ray diffraction analysis (see Chap.4

The oscillations in the asymmetry curves indicating the internal magnetic

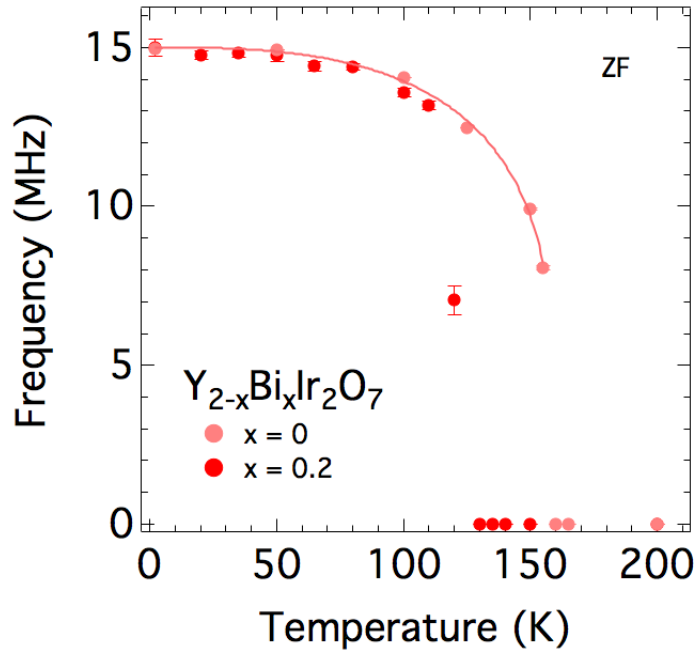


Figure 5.2: Temperature dependence of the frequency parameter obtain from the fitting of the μSR data using Eq. 5.1 as shown in Fig.5.1. It can be seen that the frequency does not change with the input of bismuth but the transition temperature decreases. This order parameter is fitted using a phenomenological equation $\langle B_{loc} \rangle \sim [1 - (T/T_c)^\alpha]^\beta$.

field due to long range order are not seen in the 0.4 sample. To rule out the possibility of small oscillations to be hidden by the background noise very high statistics (40M counts) were taken on one of the $x = 0.4$ samples at base temperature (2.2 K). The absence of oscillation in this sample means that the long range magnetic order is very quickly destroyed by the presence of the bismuth. 20% of bismuth is enough to suppress the order. For completeness the 0.9 and 1.3 samples were measure with μSR . The 0.9 sample shows evidence of oscillations and that is in agreement with the previous statement that in reality this sample actually has a doping of 15% ($x \sim 0.3$). The frequency is the same as the one measured for the pure and first doped sample

but the amplitude is smaller than $x = 0.2$.

5.1.2 Weak transverse field and transversed field

For a better understanding of the paramagnetic volume fraction in each of the $Y_{2-x}Bi_xIr_2O_7$ samples a weak transverse field (WTF) scan was done. The sample mounting and instruments were the same as for the ZF set up except that a weak vertical magnetic field was applied. The data from the weak transversed field was again fit using the program MSRFIT. The function used to fit all temperatures for all concentrations (0.2, 0.4, 0.9 and 1.3) is a simple precession function with an exponential envelope

$$P(t) = A_1 \exp(-\lambda_1 t) \cos(\omega_\mu t + \phi) \quad (5.2)$$

Each run was fitted individually with no common or fixed parameters .

The asymmetry data (Fig. 5.3) shows that the paramagnetic phase becomes larger as the doping of bismuth increases, supporting the idea of the order phase being destroyed by the dopant ion. As expected, above the transition temperature the asymmetry for all samples is the same (~ 0.2) as the samples become paramagnetic. In Fig. 5.3 it can be seen what fraction of the sample is paramagnetic. For the lowest temperature value (2 K) of the $x = 0.2$ sample (asymmetry ~ 0.07), the paramagnetic phase is $\sim 35\%$ of the high temperature value (180 K). With only 10% of yttrium substituted by bismuth, $\sim 35\%$ of the sample is paramagnetic and thus only $\sim 65\%$ possess large state internal fields. The situation is more drastic on the 0.4 sample in which with only 40% of bismuth, the paramagnetic volume fraction at the lowest temperature (2 K) is $\sim 70\%$. Now it can be understood why the ampli-

tude of the muon oscillation signal decreased so rapidly with doping. In the $x = 0.4$ sample no evidence of large static fields are seen because only 30% of the sample is non paramagnetic with antiferromagnetic ordering.

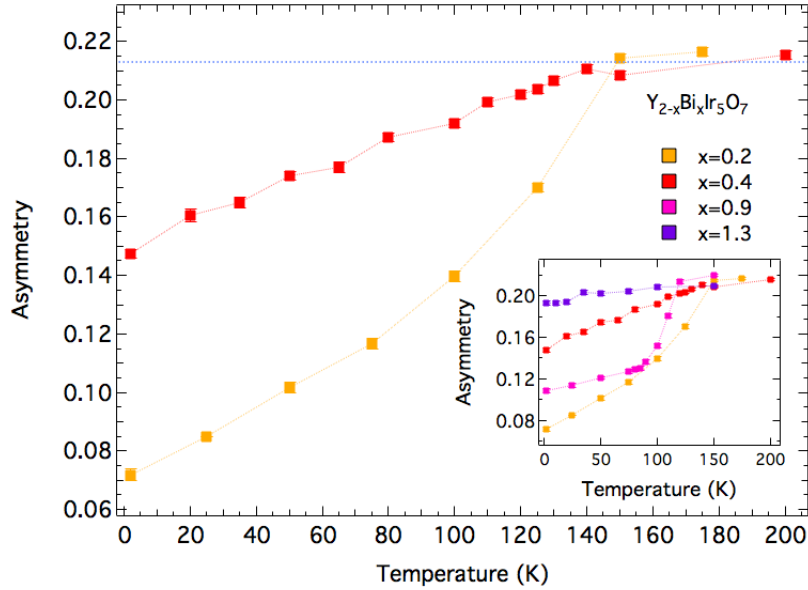


Figure 5.3: Asymmetry derived from the fitting of the μSR weak transverse field data using equation 5.2 for the $x = 0.2$ and 0.4 . The dotted line is a guide to the line to see the value of the asymmetry above the transition temperature where all the sample is the paramagnetic. The rest of the doped samples which were determined of not good quality ($x = 0.9$ and 1.3) are shown in the inset of the graph to compare.

Turning now the attention to the higher doped samples plotted in the inset of Fig. 5.3, it can be seen that the paramagnetic volume fraction is consistent with the previous results showing a $x = 0.9$ sample that has less paramagnetic volume fraction than expected and more like the estimated percentage of bismuth substitution as shown in Tab. 4.4. The same behaviour is seen for the highest doped sample where the asymmetry behaves more like a less doped sample.

5.2 Bi₂Ir₂O₇ results

The substitution of bismuth in the Y₂Ir₂O₇ structure and the subsequent destruction of the magnetic order is to be expected in the fully doped sample as said in the introductory chapter (chap. 1). The destruction of the magnetic order is an interesting phenomena and has been the focus of intensive study and controversy. In this work μSR experiments were conducted in a Bi₂Ir₂O₇ sample at low temperatures to determine whether or not there is phase transition into a magnetic ordered state.

The sample that was sintered into a thin disc was mounted in a DR cryostat where the first measurements were zero field μSR measurements. To study the behaviour of the sample the data was fit to a Gaussian Kubo-Toyabe polarisation function:

$$P(t) = \frac{1}{3} + \frac{2}{3}(1 - \Delta^2 t^2) \exp(-\frac{1}{2}\Delta^2 t^2). \quad (5.3)$$

This function is used for systems that possess randomly oriented spins where the width of the local field distribution is represented by the Gaussian of width Δ . In the asymmetry of the ZF data there was no sign of oscillations as shown in Fig.5.4. This was expected and corroborates the idea of no magnetic order in the system. The asymmetry spectra shows no difference between the highest temperature (5 K) and the lowest measured (30 mK). The relaxation parameter obtained from the fitting was plotted against temperature to see its evolution (Fig. 5.5). No changes with temperature were seen in the behaviour of the relaxation down to 30 mK. The results confirmed the behaviour proposed for this system [Qi 2012] as well as agreeing with the previous results obtained in this work. However a published work by Baker *et al.* reports two

transitions at low temperatures that were not previously predicted. These results are in contradiction with this work, as the data for the zero field shows a lack of features in the asymmetry and relaxation, indicating that there is no presence of static order of dynamic relaxation down to 30 mK (Fig. 5.5). We note that the relaxation seen by Baker *et al.* is very small and in view of our results may be extrinsic.

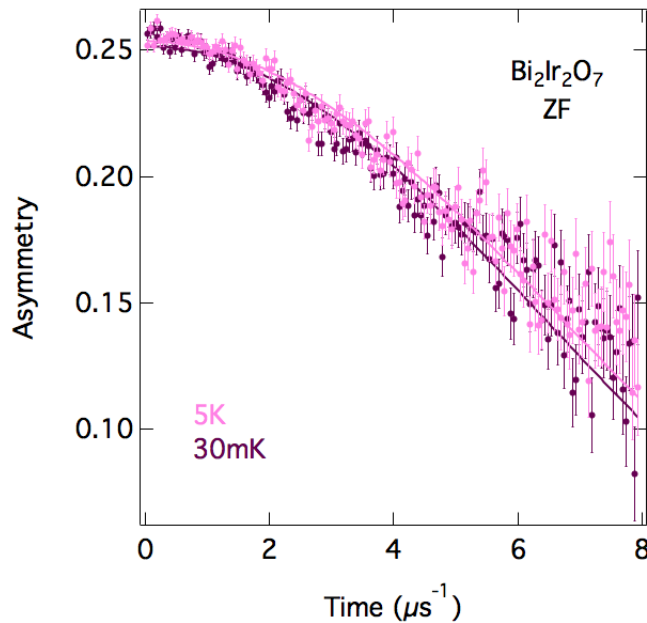


Figure 5.4: Zero field μSR data of the fully doped bismuth iridate that was been fitted to Eq. 5.3. For comparison the higher temperature (5 K) and the lower temperature (30 mK) measured have been plotted together and it can be seen that there is no difference between them. There is no evidence of a transition to an ordered state.

In addition to the ZF study, TF measurements were conducted on the fully doped sample, $\text{Bi}_2\text{Ir}_2\text{O}_7$, to measure the Knight shift. A field of 1T was applied perpendicular to the direction of the muon spin as explained in chapter 3. The data was again fit with a simple precession function with an exponential envelope (Eq. 5.2) using a rotating reference frame. The use of

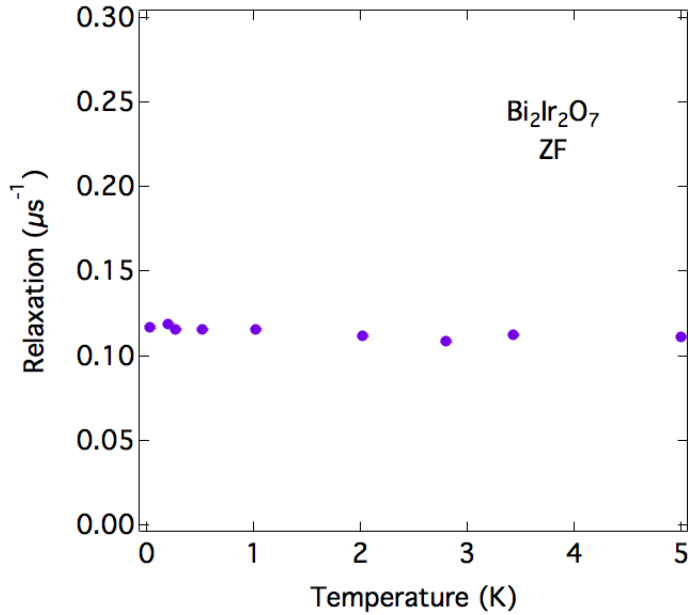


Figure 5.5: Plot of the relaxation (λ) obtain from the fitting of the zero field μSR data of the $\text{Bi}_2\text{Ir}_2\text{O}_7$ using equation 5.3. The relaxation shows no evidence of a transition temperature

rotational reference frame was required in the analysis of the data to be able to observe the oscillations as the muons precess at a very high frequency (134 MHz).

The asymmetry for the higher and lower temperature shows oscillations due to the external field applied (Fig. 5.6). Now the interest lies in the study of the Knight shift. The frequency of the oscillations seen in the asymmetry signal can differ from that expected for the externally applied field, due to local susceptibility. The frequency vs. temperature plot (Fig. 5.7 (a)) reveals a flat profile except for the 5 K point, where the frequency is slightly (2×10^5) higher. The flat profile was to be expected as no magnetic transition was anticipated. Thus a close look of the to the 5 K point was needed. To investigate the reason of the difference of the 5 K point a comparison of the

muon spin frequency obtained from the fitting of the data is compared to the measured field in the magnet using a hall probe. The values of the field measured with a Hall probe plotted against the temperature also show an increase at the 5 K (Fig. 5.7 (b)) indicating that the field being applied was of a slightly higher value. The reason for this is that the 5 K measurement was the first point to be measured and there was some slight relaxation of the field in the time required to cooled the sample from 5 K to 30 mK.

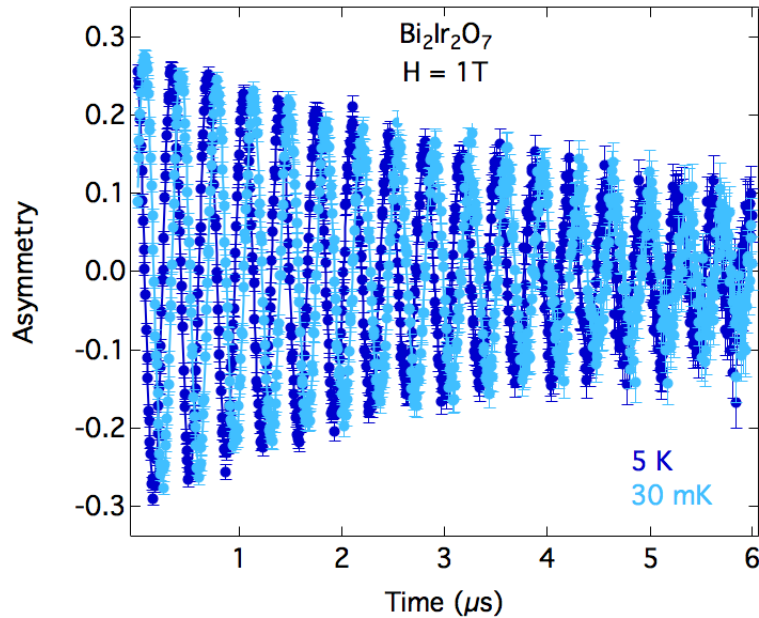


Figure 5.6: 1tesla transversed field μSR data with fits to equation 5.2 on $\text{Bi}_2\text{Ir}_2\text{O}_7$. Plotted are the 5 K and 30 mK signals for a comparison. No difference can be seen between the two samples confirming the absence of transition into a ordered state.

The plot of the ratio of the frequency over the measured Hall probe field (f/H) vs. temperature shows a linear behaviour increasing with temperature but also shows a bigger value of the field at the 5 K point. This means that the conclusion arrived for the sudden increase on frequency seen in the frequency graph at the 5 K point (Fig. 5.7 (a)) was most probably caused

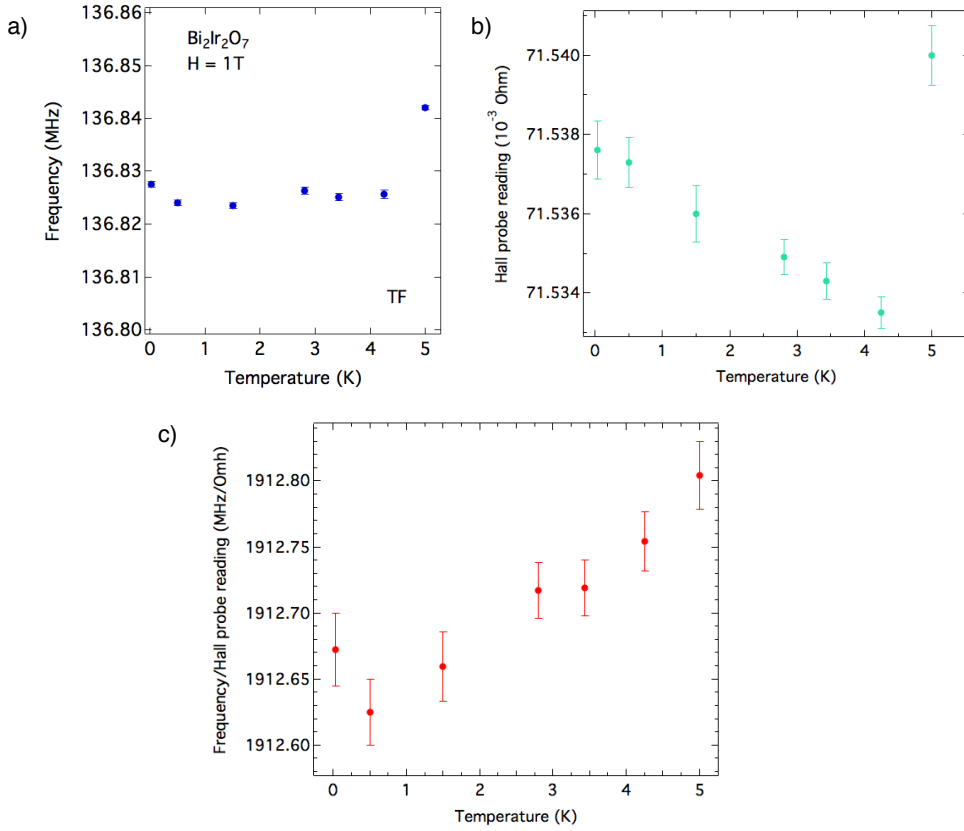


Figure 5.7: Parameters derived from fitting the data in Fig.5.6 using equation 5.2. (a) In the frequency vs. temperature a flat profile is seen except for the point at 5 K that seems to be a little higher due to the magnetic field not being stabilised. (b) To check approximately what was the field that was being applied to the sample, the hall probe measurement is plotted against temperature to see the field value at each moment. It can be seen that the value of the field at 5K is a little higher that expected. (c) To see if the field stabilisation affected the measurements, the ratio of the frequency over the Hall probe reading is plotted against the temperature. The linear increase shows that though the value of the field was not the correct one, the Knight shift increases with temperature is smooth and proportional to the internal field induced.

by flux in the superconducting magnet. In fact the Hall probe field decreases monotonically in time (measurement sequence was $T = 5\text{ K}$, 30 mK and then increasing temperature). This finding takes out of the equation the possibility of a magnetic phase change. In the graph of f/H vs. temperature (Fig. 5.7 (c))

it can be seen that there is a small Knight shift that increases with decreasing temperature as the plot is not a straight line but has a linear behaviour. The Knight shift is proportional to the susceptibility of the system. Recalling the susceptibility data in Fig.4.1. In that figure the susceptibility of the $\text{Bi}_2\text{Ir}_2\text{O}_7$ increases with decreasing temperature in agreeing with the μSR results.

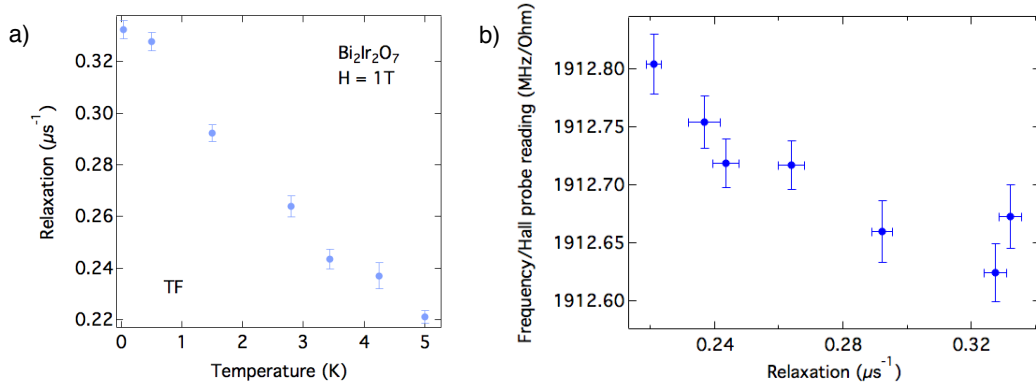


Figure 5.8: (a) The increase of the relaxation of the μSR data with decreasing temperature indicates a broadening of the angular variation in the susceptibility which is proportional to the internal inhomogeneous field. (b) In the frequency-Hall probe ratio vs. relaxation plot it can be seen that the knight shift is proportional to the broadening. This means that the broadening increases with the shift.

There is a weak temperature dependance of the relaxation of the $\text{Bi}_2\text{Ir}_2\text{O}_7$ system in the 1T transverse field with increased relaxation with decreasing temperature. We see (Fig.5.8 (b)) that the relaxation and normalised frequency shift are linearly related, indicating that the broadening is likely a T_2 effect due to angular averaging of the Knight shift in our powder sample. The broadening is proportional to the angular variation of the susceptibility. These results for $\text{Bi}_2\text{Ir}_2\text{O}_7$ show that this material remains paramagnetic down to at least 30 mK.

Conclusions and future work

Contents

| | |
|--|-----------|
| 6.1 Prospective future work | 73 |
|--|-----------|

In this thesis we presented a study of the magnetic properties of $\text{Y}_{2-x}\text{Bi}_x\text{Ir}_2\text{O}_7$ $x = 0, 0.2, 0.4, 0.9, 1.3$ and 2 . The polycrystalline samples were synthesized at Stanford University by stoichiometric mixtures of the respective starting oxides (Eq. 4.1) and annealed repeatedly until the desired phase was realised. For the doped samples some problems were encountered due to incomplete reactions. This problem was discovered after carrying X-ray refinements on the samples. Previous work had shown that with the addition of bismuth to the $\text{Y}_2\text{Ir}_2\text{O}_7$ structure there was a linear increase of lattice parameters [Aito 2003] (Vegard law). The X-ray refinement was done with the purpose of serving as a first assessment of the quality of the samples. From this refinement it was concluded that only the low doping samples ($x = 0, 0.2$ and 0.4) had the correct phase and no evidence of secondary magnetic phases (Fig. 4.4).

For a first general characterisation of the magnetic properties of the system, DC magnetic susceptibility was performed. These data showed the existence of a magnetic transition to an ordered state (Fig. 4.1). The transition temperature decreases with the addition of bismuth. The susceptibility also

showed the presence of a weak ferromagnetic component to the order which appears as a difference between the zero field cooled signal that stays constant in temperature and the field cooled signal that increases below the transition temperature. These results are in agreement with previous results ([Aito 2003]) and the belief that this family of samples order in an antiferromagnetic fashion with canted spins that give rise to the weak ferromagnetic signal [Fukazawa 2002] [Matsuhira 2011].

Thanks to the μSR study it could be seen that there is order in the $Y_2Ir_2O_7$ and $x = 0.2$ samples as an internal field at the muon stopping site is measured in the zero field set up (Fig. 5.1 and 5.2). The presence of the field is a direct evidence of a field created due to the frozen spins. By measuring the internal field in these samples two things could be seen. First, the field amplitude does not decrease with addition of bismuth. And second the transition temperature, as seen in the susceptibility measurements, decreases with doping until for the $x = 0.4$ sample no internal field is detected. Combining the information gain from the zero field measurements with the weak transverse field measurements (Fig. 5.3) it can be seen that when the bismuth is added into the $Y_2Ir_2O_7$ system the paramagnetic volume fraction is increased as seen in the WTF data but this does not change the internal local field at low temperatures measured with the ZF set up.

Our susceptibility and μSR measurements of $Bi_2Ir_2O_7$ showed that the bismuth iridate system remains paramagnetic with no transition temperature into an ordered state (Fig. 5.5) down to 30 mK. Though other groups have seen evidence of a magnetic transition for $Bi_2Ir_2O_7$ at low temperatures [Baker 2013], the existence of such a transition could not be seen either in the zero field or transverse field μSR measurements nor the susceptibil-

ity measured for this work. The transverse field measurement (Fig. 5.7) of bismuth iridate showed a small Knight shift.

With the results obtain in this work the phase diagram published by Matsuhira *et al.* [Matsuhira 2011] can be expanded to include yttrium and bismuth (Fig.6.1)

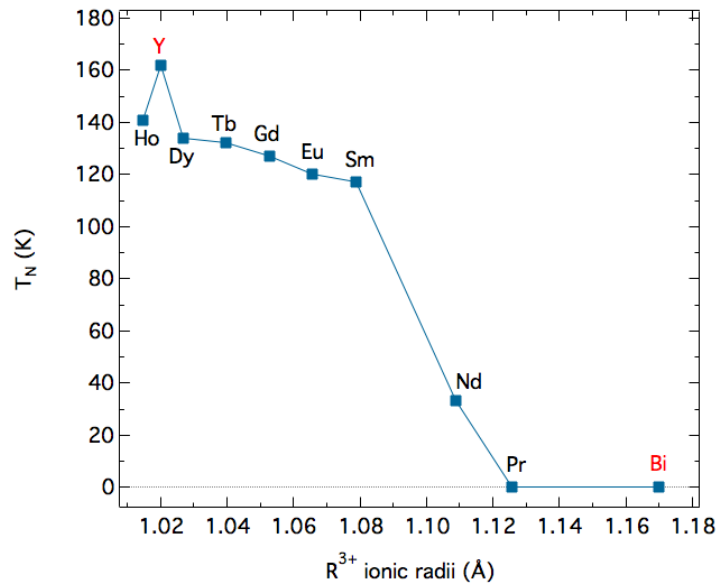


Figure 6.1: Phase diagram of $R_2Ir_2O_7$ based on R site ionic radius dependence of the metal-insulator transition and magnetic transition temperature.

6.1 Prospective future work

To further understand this system and the problems that have showed up, new samples of $x = 0.9$ and 1.3 have just been synthesized at Stanford University after a few months of work. The measurements planned for the new samples are: first an assessment of quality with X-ray diffraction to check that the samples are free of secondary phases and that the lattice parameters take the correct value. Then susceptibility and μSR measurement will be carried out in

the same conditions as the other samples to check that there is consistency in the results and the predictions based on the data already acquired is realised. The prediction is that they will have a lower transition temperature and no evidence of a uniform internal magnetic field due to the level of bismuth substitution.

For the $\text{Bi}_2\text{Ir}_2\text{O}_7$ system new measurements have been done that need to be analysed. There is DC susceptibility data done at several fields (100 G, 500 G, 10 KG and 40 KG) as well as very recent μSR data on high fields (1 T, 4 T and 6 T). The susceptibility data that was taken prior to the μSR experiment showed that the susceptibility at low temperatures a turnover that had never be seen before (Fig. 6.2). Because this turnover does not have a consistent behaviour (it is not present in the 500 G measurement) and its origin is not well understood and at this moment more susceptibility measurements are been taken. The early results from μSR relaxation of the transverse field measurements, show that there is a turn over of the relaxation for the 4 T signal. At this stage of the analysis nothing else can be said with regards to these new results but after their full analysis the hope is to obtain a unified picture of this yttrium iridate system doped with bismuth.

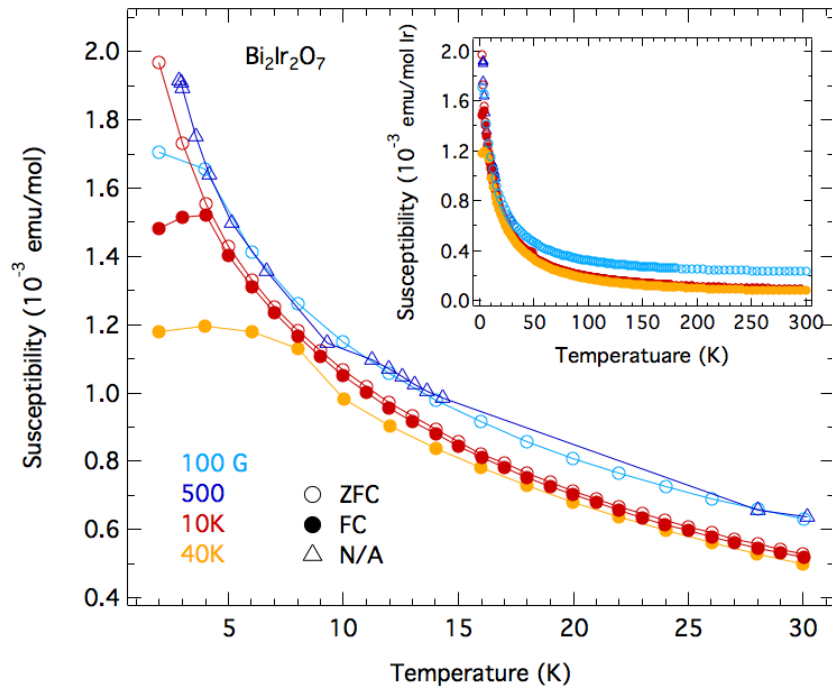


Figure 6.2: Plot of the magnetic susceptibility on the $\text{Bi}_2\text{Ir}_2\text{O}_7$ in 100 G, 500 G, 10 KG and 40 KG fields. Zero field cooled (ZFC) or field cooled (FC) measurement were done at those fields but in the case of 1 T were both FC and ZFC measurements were taken. A distinct turn over is observed for three of the four fields measured. The inset shows the behaviour of this sample at high temperatures for each of the fields.

Bibliography

- [Aito 2003] Natsuki Aito, Minoru Soda, Yoshiaki Kobayashi and Masatoshi Sato. *Spin–Glass-like Transition and Hall Resistivity of $Y_{2-x}Bi_xIr_2O_7$* . Journal of the Physical Society of Japan, vol. 72, no. 5, pages 1226–1230, 2003. (Cited on pages [41](#), [71](#) and [72](#).)
- [Ashcroft 1981] Neil W Ashcroft and N David Mermin. *Solid State Physics (Saunders College, Philadelphia, 1976)*. There is no corresponding record for this reference, pages 673–674, 1981. (Cited on page [21](#).)
- [Baker 2013] PJ Baker, JS Möller, FL Pratt, W Hayes, SJ Blundell, Tom Lancaster, TF Qi and Gang Cao. *Weak magnetic transitions in pyrochlore $Bi_2Ir_2O_7$* . Physical Review B, vol. 87, no. 18, page 180409, 2013. (Cited on pages [6](#), [13](#) and [72](#).)
- [Blundell 2012] SJ Blundell, AJ Steele, T Lancaster, JD Wright and FL Pratt. *A Bayesian Approach to Magnetic Moment Determination Using μ SR*. Physics Procedia, vol. 30, pages 113–116, 2012. (Cited on page [10](#).)
- [Clarke 2006] John Clarke and Alex I Braginski. The squid handbook. Wiley Online Library, 2006. (Cited on pages [vii](#), [16](#), [17](#) and [19](#).)
- [Cukauskas 1974] Edward J Cukauskas, Daniel A Vincent and Bascom S Deaver Jr. *Magnetic susceptibility measurements using a superconducting magnetometer*. Review of Scientific Instruments, vol. 45, no. 1, pages 1–6, 1974. (Cited on pages [20](#) and [24](#).)
-

- [Design 2013] Quantum Design. *Magnetic property measurement system. Hardware reference manual*. Quantum Design, 6325 Lusk Boulevard, San Diego, CA 92121, January 2013. (Cited on pages vii and 21.)
- [Disseler 2012] SM Disseler, Chetan Dhital, A Amato, SR Giblin, Clarina de la Cruz, Stephen D Wilson and MJ Graf. *Magnetic order in the pyrochlore iridates $A_2Ir_2O_7$ ($A = Y, Yb$)*. Physical Review B, vol. 86, no. 1, page 014428, 2012. (Cited on pages 7, 9, 10 and 58.)
- [Disseler 2014] Steven M Disseler. *Direct evidence for the all-in/all-out magnetic structure in the pyrochlore iridates from muon spin relaxation*. Physical Review B, vol. 89, no. 14, page 140413, 2014. (Cited on pages 6, 9 and 10.)
- [Fukazawa 2002] Hideto Fukazawa and Yoshiteru Maeno. *Filling control of the pyrochlore oxide $Y_2Ir_2O_7$* . Journal of the Physical Society of Japan, vol. 71, no. 10, pages 2578–2579, 2002. (Cited on pages 8, 9, 11, 12 and 72.)
- [Gardner 2010] Jason S Gardner, Michel JP Gingras and John E Greedan. *Magnetic pyrochlore oxides*. Reviews of Modern Physics, vol. 82, no. 1, page 53, 2010. (Cited on pages 4, 5, 6 and 8.)
- [Greedan 1994] John E Greedan. *Magnetic oxides*. Encyclopedia of Inorganic and Bioinorganic Chemistry, 1994. (Cited on page 11.)
- [Kreitzman 1999] S Kreitzman, Donald J Arseneau, Bassam Hitti and Jess H Brewer. *μ SR Facility Users Guide*, 1999. (Cited on pages viii, 33 and 39.)

- [Lacroix 2011] Claudine Lacroix, Philippe Mendels and Frederic Mila. Introduction to frustrated magnetism: Materials, experiments, theory, volume 164. Springer, 2011. (Cited on page 5.)
- [Matsuhira 2007] Kazuyuki Matsuhira, Makoto Wakeshima, Ryo Nakanishi, Takaaki Yamada, Akira Nakamura, Wataru Kawano, Seishi Takagi and Yukio Hinatsu. *Metal-Insulator Transition in Pyrochlore Iridates $Ln_2Ir_2O_7$ ($Ln = Nd, Sm, \text{ and } Eu$)*. Journal of the Physical Society of Japan, vol. 76, no. 4, 2007. (Cited on page 7.)
- [Matsuhira 2011] Kazuyuki Matsuhira, Makoto Wakeshima, Yukio Hinatsu and Seishi Takagi. *Metal-Insulator Transitions in Pyrochlore Oxides $Ln_2Ir_2O_7$* . Journal of the Physical Society of Japan, vol. 80, no. 9, 2011. (Cited on pages 8, 9, 72 and 73.)
- [Nagamine 2003] Kanetada Nagamine and Kanetada Nagamine. Introductory muon science, volume 208. Cambridge University Press Cambridge, 2003. (Cited on page 27.)
- [Qi 2012] TF Qi, OB Korneta, Xiangang Wan, LE DeLong, P Schlottmann and G Cao. *Strong magnetic instability in correlated metallic $Bi_2Ir_2O_7$* . Journal of Physics: Condensed Matter, vol. 24, no. 34, page 345601, 2012. (Cited on pages 7, 12, 13 and 64.)
- [Shannon 1976] RD t Shannon. *Revised effective ionic radii and systematic studies of interatomic distances in halides and chalcogenides*. Acta Crystallographica Section A: Crystal Physics, Diffraction, Theoretical and General Crystallography, vol. 32, no. 5, pages 751–767, 1976. (Cited on pages 12 and 45.)

[Shapiro 2012] Max C Shapiro, Scott C Riggs, Matthew B Stone, Clarina R de la Cruz, Songxue Chi, Andrey A Podlesnyak and Ian R Fisher. *Structure and magnetic properties of the pyrochlore iridate $Y_2Ir_2O_7$* . Physical Review B, vol. 85, no. 21, page 214434, 2012. (Cited on pages 8, 46 and 47.)

[Shoemaker 2011] Daniel P Shoemaker, Ram Seshadri, Makoto Tachibana and Andrew L Hector. *Incoherent Bi off-centering in $Bi_2Ti_2O_6O'$ and $Bi_2Ru_2O_6O'$: Insulator versus metal*. Physical Review B, vol. 84, no. 6, page 064117, 2011. (Cited on page 44.)

[Soda 2003] M Soda, N Aito, Y Kurahashi, Y Kobayashi and M Sato. *Transport, thermal and magnetic properties of pyrochlore oxides $Y_{2-x}Bi_xIr_2O_7$* . Physica B: Condensed Matter, vol. 329, pages 1071–1073, 2003. (Cited on page 41.)

[Sonier] J Sonier. *Muon spin rotation/relaxation/resonance (μ SR)*. (Cited on pages viii, 28, 30, 31, 32 and 37.)

[Tinkham 2012] Michael Tinkham. Introduction to superconductivity. Courier Dover Publications, 2012. (Cited on page 16.)

[Yanagishima 2001] Daiki Yanagishima and Yoshiteru Maeno. *Metal-nonmetal changeover in pyrochlore iridates*. Journal of the Physical Society of Japan, vol. 70, no. 10, pages 2880–2883, 2001. (Cited on pages 7, 8 and 41.)

[Yaouanc 2011] Alain Yaouanc and Pierre Dalmas De Réotier. Muon spin rotation, relaxation, and resonance: Applications to condensed matter.

Numeéro 147. Oxford University Press, 2011. (Cited on pages 28, 36 and 38.)